Journal of Cleaner Production 518 (2025) 145908

Contents lists available at ScienceDirect

Journal of Cleaner Production

journal homepage: www.elsevier.com/locate/jclepro

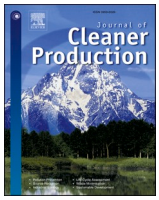

Effect of water washing on pyrolysis of Shaerhu coal and prediction of sodium and chloride release using neural network model

Zhihua Tian [1], Ruiqing Jia [1], Bin Zhang [1], Qinhui Wang [*]

State Key Laboratory of Clean Energy Utilization, Zhejiang University, Hangzhou, 310027, China

ARTICLE INFO

Keywords:
Coal
Washing
Pyrolysis
Char characteristics
Neural network
Prediction

ABSTRACT

Coal consistently plays a major role in global energy consumption. With high-quality coal reserves dwindling, low-cost, abundant high-sodium coal has attracted attention despite challenges posed by Na and Cl release during thermal utilization, which can lead to equipment corrosion. This study investigated the pyrolysis of high-sodium Shaerhu coal (SEH) from Xinjiang in a fluidized bed. Results showed that water washing significantly reduces water-soluble Na and Cl, decreasing their content to 764 μg g^{-1} and 698 μg g^{-1}, respectively, after 120 min. Compared to unwashed coal, washed coal (WS) demonstrates increased char yield and ash melting point, alongside reduced char reactivity and Na and Cl release. Characterization by Raman, XRD, and FTIR reveals changes in char's graphitization, microcrystalline structure, and functional groups with washing time. BET analysis indicates reduced adsorption and specific surface area in WS char. A neural network model developed for predicting Na and Cl release during pyrolysis achieved an error margin within 5 %. These findings provide critical data and theoretical support for optimizing the pyrolysis process of high-sodium coal.

1. Introduction

Coal remains a critical global energy resource, widely utilized across sectors such as electricity generation, steel production, and chemical industries (Wan et al., 2017). Currently, around 40 % of the world's electricity is generated from coal (Khatami and Levendis, 2016). However, as high-quality coal resources become increasingly scarce, attention has shifted towards abundant and cost-effective low-rank coals, which are rich in alkali metals (Wu et al., 2016; Liu et al., 2018a; Wang et al., 2017). Notably, the Zhundong area in northwestern China holds coal reserves estimated at 390 billion tons, primarily comprising high-sodium, low-rank coal (Lou et al., 2021; Li et al., 2018). This supply alone could potentially meet China's energy needs for over a century at the current consumption rate (Song et al., 2016a). Low-rank, high-sodium coal is considered a valuable resource mainly because of its large reserves. Low-rank, high-sodium coal reserves in China reach 390 billion tons. Abundant low-rank, high-sodium coal deposits around the world, like those in the Zhundong area, ensure a stable long - term energy supply. Economically, its relatively low cost of extraction and acquisition makes it an attractive option for large - scale energy production, which can effectively reduce the economic cost of energy production. In terms of energy, although its quality is relatively poor, through technologies such as pyrolysis and gasification, it can be converted into various energy products, which can be used for power generation and chemical raw materials, expanding the energy supply channels and playing a crucial role in the energy diversification strategy. Therefore, with its substantial economic and energy potential, high-sodium, low-rank coal is a valuable resource (Wang et al., 2015a; Zhang et al., 2022a). However, in practical applications, the presence of sodium leads to a series of problems in boilers, such as slagging and corrosion, directly impacting the safety and economic efficiency of its thermal utilization process (Ding et al., 2019). Therefore, significant constraints limit the effective utilization of high-sodium, low-rank coal (Wen et al., 2017; Zhu et al., 2019).

Recent studies have focused increasingly on high-sodium coal, particularly sodium's forms and its migration behavior during combustion and pyrolysis. Sodium in coal is present in four forms, water-soluble, acetic acid-soluble, hydrochloric acid-soluble, and insoluble sodium (Song et al., 2016b). Under high-temperature conditions, Na release mainly originates from W-Na in coal, which can deposit on equipment heat-exchange surfaces as sodium chloride or sodium sulfate, leading to metal corrosion (Xu et al., 2018a; Chen et al., 2020).

* Corresponding author.
E-mail address: qhwang@zju.edu.cn (Q. Wang).
[1] These authors contributed equally to this work.

https://doi.org/10.1016/j.jclepro.2025.145908
Received 16 January 2025; Received in revised form 29 April 2025; Accepted 1 June 2025
Available online 3 June 2025

Conversely, insoluble sodium remains largely in char (Wang et al., 2015b). Although sodium release may damage equipment, some researchers have observed that sodium in coal can influence coal reactivity and gas product composition (Zhang et al., 2020). Additionally, interactions between sodium and other mineral elements (e.g., silicon, aluminum, iron) in coal are drawing attention. These elements can impact sodium migration and deposition (Song et al., 2017). A deeper understanding of these reactions and transformations is vital for effective sodium release control.

Recent studies have found (He et al., 2023a; Zhu et al., 2022) that the release of Na and Cl is highly temperature-dependent and strongly affected by their chemical form and their interaction with the minerals in the coal, especially in the pyrolysis of low-rank coal in the Zhundong region. Studies have shown that water washing pretreatment can effectively remove water-soluble alkali and halogen substances, reduce their release during thermal conversion, and thus reduce the risk of slagging and corrosion (Liu et al., 2018b; Niu et al., 2019; Hui et al., 2021). Recent studies (Chen et al., 2025; Peng et al., 2018) have explored the transformation mechanism of Na and Cl, indicating that Na may be converted into less volatile compounds by reacting with aluminosilicates, while Cl mainly volatilizes in the form of HCl or alkali metal chlorides. Ma et al. (2025) also studied the evolution of Cl during coal pyrolysis and observed that most of the Cl released during low-temperature pyrolysis is water-soluble Cl. Meanwhile, data-driven methods have developed rapidly in the field of coal combustion and pyrolysis. Artificial neural networks (ANN) are increasingly used to predict related dependent variables under different operating conditions because of their ability to capture multivariate interactions (Asani et al., 2023; Oyekunle et al., 2025). Some recent studies have shown (Obafemi et al., 2019; Sunphorka et al., 2017) that machine learning and ANN can accurately predict some important parameters and characteristics of coal pyrolysis and combustion, which can provide methods and basis for intelligent control of coal thermal utilization processes.

Previous studies (Cao et al., 2024; Zhu et al., 2017; Wang et al., 2018; Lin et al., 2018) on high-sodium coal have mainly focused on the migration behavior of Na and Cl during its combustion and pyrolysis. However, there are still some shortcomings. First, few studies have systematically investigated how water washing changes the forms of Na and Cl and their release during pyrolysis. Moreover, the effects of Na and Cl content and water washing on the microstructure and reactivity of char are not very clear. Finally, existing prediction models usually rely on simplified empirical relationships, which limits their applicability under complex conditions. This study will address these gaps by combining experimental studies and neural network modeling. The results of this study clarify the effects of water washing and Na and Cl content on the pyrolysis process and char, and achieve the prediction of Na and Cl release during the pyrolysis of high-sodium coal.

To address the pressing challenges of thermal utilization of high-sodium coal with high reserves and low cost, especially its tendency to release corrosive Na and Cl species, a deeper understanding of the influence of pretreatment processes such as water washing on the characteristics of pyrolysis products and the release behavior of Na and Cl is essential. However, the current research on the relationship between the change of Na and Cl speciation caused by water washing and its effect on pyrolysis behavior is still limited. Moreover, most of the existing studies rely on empirical observations and may not effectively capture the multi-factor interactions that affect the release of elements. In addition, despite the increasing application of machine learning methods such as neural networks in coal science, there are few studies combining them with experimental data to predict the release of Na and Cl during pyrolysis of high-sodium coal. Therefore, this study aims to bridge this gap and will systematically study the effects of water washing on Na and Cl speciation, pyrolysis process and char structure. Meanwhile, this study will construct a neural network model that can accurately predict the release behavior of Na and Cl under different conditions. This comprehensive approach aims to provide a predictive tool for the clean and intelligent utilization of high-sodium coal in industrial applications.

2. Experimental methods

2.1. Coal and experimental equipment

This study used Shaerhu coal (SEH), sourced from Xinjiang province, China. SEH coal is a low-rank, high-alkali coal with high content of Na and Cl. The coal was ground to a particle size under 0.15 mm, then dried. Then, 0.1 g of the dried sample was digested, and the solution was diluted to 100 mL with deionized water. Sodium content of solution was determined by ion chromatography, yielding a Na concentration in SEH. Using the potassium thiocyanate titration method outlined in GB/T 3558-1996, the Cl content in SEH was measured. Experimentally, Na and Cl contents were found to be 8165 μg g^{-1} and 6560 μg g^{-1}, respectively. According to MT/T 1074–2007 (a) and GB/T 20475.2-2006 (b) standards, when the Na content in coal is higher than 0.5 %, the coal is classified as high-sodium coal, and when the Cl content is higher than 0.3 %, the coal is classified as high-chlorine coal. Therefore, SEH is high-sodium and high-chlorine coal.

Before experimentation, SEH was pretreated. Appropriate washing conditions are essential for the effective removal of alkali metals and halogen elements. According to previous studies, Wang et al. (2016) found that washing temperatures in the range of 40–60 °C can improve the efficiency of washing. Guo et al. (2017a) found that the Na content in coal hardly changes after the washing time reaches 3 h. Zhao et al. (2014) found that washing high-sodium coal at a solid-liquid ratio of 1:10 can not only ensure the washing effect, but also reduce the use of deionized water and thus reduce costs. Therefore, using a thermostatic magnetic stirrer in this washing progress, 20 g of sieved, dried SEH was placed in a beaker with deionized water at a solid-to-liquid ratio of 1:10 for washing. The mixture was stirred at 50 °C and 500 rpm. The washing time of the coal in this experiment was selected as 0–120 min. After stirring for the set duration, the solution was filtered, and the washed coal sample was dried in an oven at 105 °C for 12 h. Elemental, proximate, and ash analyses were conducted on both SEH and coal washed for 120 min (WS). The results were summarized in Tables 1 and 2.

Table 3 shows the contents of water-soluble sodium (W-Na), hydrochloric acid-soluble sodium (H-Na), acetic acid-soluble sodium (A-Na), insoluble sodium (I-Na), water-soluble chlorine (W-Cl), and insoluble chlorine (I-Cl) in SEH and WS. Wijaya et al. (2011) found that washing with deionized water would reduce the Cl content by 80 %–90 %. Related studies (Guo et al., 2017a; Zhao et al., 2014; Quast, 2000) have shown that washing will remove 45 %–65 % of Na. Zhu et al. (2017) found that most of the Na removed during the water washing process was W-Na. In this study, the W-Na content in the coal samples after water washing was reduced by more than 80 %, and the W-Cl content was reduced by about 90 %. This experimental result is consistent with previous research reports. It also proves that the water washing parameters used in this study can effectively remove most of the easily releasable Na and Cl in high-sodium coal.

A small bubbling fluidized bed equipped with a tail gas collection system served as the reactor, which included an air supply, temperature control, and a primary reaction chamber. The reaction chamber consisted of a 1200 mm quartz tube with a 3 mm thick distributor plate located 500 mm from the base. The distributor plate contained 0.5 mm holes spaced 0.8 mm apart. The quartz tube was vertically installed in an electric furnace, and its temperature was controlled by a 30-segment PID programmable system. The maximum temperature for the main reaction chamber was set at 1100 °C. To prevent reactant escape, a valve system was installed at the top and a plug inserted 50 mm below. The setup is depicted in Fig. 1.

2.2. Experiment process

The raw coal was ground and sieved to a particle size below 0.15

Table 1
Proximate analysis and ultimate analysis of SHE and WS.

	Industrial analysis wt.%				Elemental analysis wt.%					Calorific value (J•g^{-1})
	M_{ad}	A_{ad}	V_{ad}	FC_{ad}	C_{ad}	H_{ad}	N_{ad}	S_{ad}	O_{ad}	
SEH	7.91	6.49	33.63	51.97	60.76	2.72	0.64	0.19	21.29	26635
WS	6.22	5.59	34.37	53.87	62.09	2.84	0.62	0.17	22.47	24967

Table 2
Ash composition of SEH and WS.

	Composition	SiO_2	Al_2O_3	Fe_2O_3	CaO	MgO	K_2O	Na_2O
SEH	wt.%	17.18	12.05	12.82	32.16	2.13	0.30	5.60
WS	wt.%	28.20	6.95	6.42	40.37	6.80	0.85	2.46

Table 3
Contents of different forms of Na and Cl in SEH and WS (μg·g^{-1}).

	W-Na	H-Na	A-Na	I -Na	W-Cl	I-Cl
SEH	5614	211	515	1825	6280	280
WS	764	157	455	1694	698	225

mm, then dried for use. The coal particle size of less than 0.15 mm was chosen to allow for more complete water washing of the coal and to increase the contact area between the coal and the reaction atmosphere, thereby promoting a more efficient and accurate pyrolysis reaction. It also ensures uniform fluidization in the experimental equipment, maintaining consistent experimental conditions. Since the temperature of coal pyrolysis in industry is usually around 700 °C, the pyrolysis temperature in this study was selected to be 500–900 °C. These temperatures range from relatively low to high, which is conducive to observing the change law of high-sodium coal at different pyrolysis stages and understanding the pyrolysis mechanism. Regarding the choice of reaction time, if the time is too short, the pyrolysis reaction will be incomplete. If the time is too long, the experimental cost will increase. According to the preliminary experiment, the mass of the char hardly changes after 20 min of pyrolysis, and the char properties are also relatively similar. Therefore, the pyrolysis time of this study is set to 20 min. This time can not only ensure that the pyrolysis reaction is fully carried out, but also simulate the actual industrial process, making the experimental results have practical value. Some of the prepared SEH samples were subjected to washing for different durations to produce water-washed coal. In each experiment, about 15 g of sample had been weighed for pyrolysis, recorded as M_{coal} (g). The fluidized bed was heated, and high-purity N_2 was used to purge the system. Once the target temperature was reached, the sample was introduced by a feeder, and the airflow rate was increased to 5 L min^{-1}, with a pyrolysis duration set to 20 min. After pyrolysis, the system had been cooled, and the remaining sample had been collected at room temperature after the quartz tube naturally cooled. The residual sample was weighed as M_{char} (g), and the char yield n_{char} (%) was calculated using Equation (1). The Na and Cl contents in the coal, labeled c_{Na} (μg•g^{-1}) and c_{Cl} (μg•g^{-1}). The Na and Cl contents in the char, labeled c'_{Na} (μg•g^{-1}) and c'_{Cl} (μg•g^{-1}), were analyzed using the previously outlined method, with Na and Cl release ratios R_{Na} (%) and R_{Cl} (%) determined by Equation (2) and Equation (3).

$$n_{Char} = \frac{M_{char}}{M_{coal}} \times 100\% \quad (1)$$

$$R_{Na} = \frac{c_{Na} - c'_{Na}}{c_{Na}} \times 100\% \quad (2)$$

$$R_{Cl} = \frac{c_{Cl} - c'_{Cl}}{c_{Cl}} \times 100\% \quad (3)$$

The samples were ground to < 0.075 mm and stored in sealed containers for later analysis. Na content in char exists in four forms: water-soluble Na, hydrochloric acid-soluble Na, acetic acid-soluble Na, and insoluble Na (Swaine, 1992). Cl content in char has two forms: water-soluble Cl and insoluble Cl. The forms of Na and Cl were analyzed using stepwise chemical extraction (Mazurek et al., 2021), where different Na forms were quantified by selective solubility in various solvents (Xu et al., 2018a). Another 1 g sample was sequentially extracted with deionized water, 1 mol L^{-1} ammonium acetate, and 1

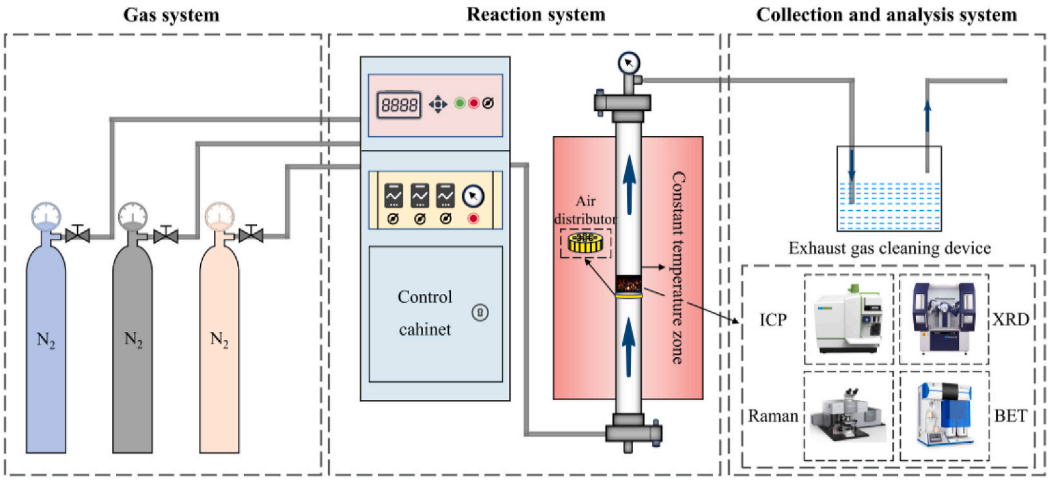

Fig. 1. A fluidized bed reactor.

mol L^{-1} HCl, then filtered. Each extract was diluted to 100 mL, and Na ion concentration q_i (μg•L^{-1}) in each solution was measured by ion chromatography. According to the measured data of Na content c_N (μg•g^{-1}) and Cl content c_C (μg•g^{-1}) in coal, this can calculate the concentrations of water-soluble Na c_W (μg•g^{-1}), ammonium acetate-soluble Na (μg•g^{-1}), and hydrochloric acid-soluble Na c_H (μg•g^{-1}) by Equation (4).

$$c_i = \frac{q_i V}{m'} \tag{4}$$

$$c_I = c_{Na} - \sum c_i \tag{5}$$

In these equations, m' (g) represents the mass of coal or char used for digestion, and V (L) is the digestion solution volume after dilution, i can represent water soluble Na, hydrochloric acid soluble Na, acetic acid soluble Na. The insoluble Na c_I (μg•g^{-1}) in the sample was calculated from the difference between the content of total Na and other forms, as shown in Equation (5).

2.3. Characterization of char

The reactivity of char, which indicates its combustion performance, was determined through thermogravimetric analysis in an air atmosphere (Xu et al., 2016). In this experiment, a Mettler TGA/DSC 3+ system was used to analyze char reactivity. 10 mg of each sample was weighed for measurement. Air with a flow rate of 100 mL min^{-1} was introduced into the instrument, and the temperature was raised to 1000 °C at a heating rate of 10 °C•min^{-1}. The temperature at which char exhibited a 50 % mass loss, recorded as $T_{0.5}$ (°C), was determined based on experimental data. The reactivity index R of char had been calculated according to Equation (6), with a higher R indicating enhanced char reactivity.

$$R = \frac{1000 - T_{0.5}}{1000} \tag{6}$$

Raman spectroscopy, sensitive to carbon structural variations, is widely applied in coal and char research for structural analysis (Xu et al., 2020; Quirico et al., 2005). In this study, a Horiba LabRAM HR Evolution Raman spectrometer measured char samples, spanning 500 - 4000 cm^{-1},with a spectral resolution of 1 cm^{-1} at a 514 nm wavelength. The Raman spectra in the 800 - 1800 cm^{-1} region were deconvoluted into 10 Gaussian peaks using ***PeakFit V4.12*** software (Quyn et al., 2002). Key parameters, such as $I_{Gr + VL + Vr}/I_D$, I_G/I_D, I_G/I_{total}, and I_S/I_G, were calculated. $I_{(Gr + VL + Vr)}/I_D$ can reflect the ratio of small aromatic ring groups to large aromatic ring groups in char (Xu et al., 2016). I_G/I_D is often used to assess carbon structure ordering and the graphitization degree is indicated by I_G/I_{total} (Li et al., 2006). I_S/I_G reflects the ratio of aliphatic to graphitic structures, with higher values suggesting a greater presence of aliphatic structures (Sun et al., 2023).

XRD analysis provides insights into the ordering of carbon atoms in coal (Johnson et al., 1986). Using a Rigaku SmartLab SE X-ray diffractometer, char samples were analyzed, with a copper X-ray source ($\lambda = 0.15405$ nm), 40 kV voltage, 40 mA current, and scan speed of $\omega = 8°$•min^{-1}, covering a 10°–80° range. Despite its amorphous nature, coal contains ordered carbon that forms microcrystalline structures. Char samples displayed diffraction peaks around 26° and 42°, labeled as the 002 and 100 peaks (Zhang and Wang, 2023). The 002 peak reflects the degree of parallel orientation of aromatic structural units. The γ band is related to the structure of aliphatic carbon (fat chain and aliphatic ring) in the molecule. The lower the degree of deterioration, the more developed the aliphatic carbon structure. Conversely, as the degree of deterioration increases, the 002 peak gradually narrows and the intensity becomes stronger, reflecting that the aromatic layer structure gradually becomes regular and orderly (Tay et al., 2013). The 100 peak is attributed to the degree of condensation of aromatic rings, that is, the size of the aromatic ring carbon network (lamellae) (Li et al., 2006). Based on the Scherrer (Xie et al., 2019) and Bragg (Zhang et al., 2017a) equations, the microcrystalline dimensions of char were calculated, as shown in Equations (7)–(9).

$$d_{002} = \frac{\lambda}{(2 \sin \theta_{002})} \tag{7}$$

$$L_c = \frac{K_1 \cdot \lambda}{(\beta_{002} \cdot \cos \theta_{002})} \tag{8}$$

$$L_a = \frac{K_2 \cdot \lambda}{(\beta_{100} \cdot \cos \theta_{100})} \tag{9}$$

In these equations, d_{002} is the distance between the aromatic monolayers in char, λ (0.15405 nm) is the wavelength of the incident X-ray, θ_{002} and θ_{100} are the grazing angles. L_c is the stacking height of the microcrystals perpendicular to the aromatic lamellae, K_1 and K_2 are the form factors ($K_1 = 0.89, K_2 = 1.84$), β_{002} and β_{100} are the half-height widths of the diffraction peaks, and L_a is the size of the microcrystals parallel to the aromatic layers. The smaller the L_a and L_c of the char microcrystals, the greater the difference between the interlayer spacing d_{002} and the interlayer spacing of the ideal graphite crystal, and the lower the degree of ordering of the microcrystal structure of the semi-coke sample. The smaller the stacking height L_a and the size L_c of char crystallite and the larger the interlayer distance d_{002}, the lower the degree of ordering of the microcrystalline structure of char (Zhang et al., 2019).

BET analysis was conducted to determine specific surface area, pore volume, and pore size distribution of char, indicating its physical and adsorptive properties. Using a Micromeritics ASAP 2460, samples were degassed at 300 °C for 7 h before testing to remove adsorbed moisture and impurities on the sample surface. N_2 adsorption-desorption was conducted at 77 K. Char with a larger surface area implies its micropore and mesopore structure were well-developed, and it has better reactivity and adsorption performance (Occelli et al., 2002). Pore size distribution impacts reaction rates and adsorption. Smaller pores enhance adsorption capacity, while larger pores aid in mass transfer (Khayet et al., 2004).

2.4. Correlation analysis and neural network models

Multiple linear regression analysis (Draper and Smith, 1998) is a statistical method used to evaluate the degree of linear correlation between multiple variables and a given outcome, suitable for investigating the presence of linear relationships between variables (Peng et al., 2023). The result of multiple linear regression is represented by the correlation coefficient r, calculated by Equation (10) (Pal and Lim, 1998). The coefficient r ranges between −1 and +1, with $r > 0$ indicating a positive correlation and $r < 0$ indicating a negative correlation (Nagelkerkea, 1991).

$$r = \frac{\sum (X - \overline{X})(Y - \overline{Y})}{\sqrt{\sum (X - \overline{X})^2} \cdot \sqrt{\sum (Y - \overline{Y})^2}} \tag{10}$$

In this equation, X and Y denote the values of two variables, while $\overline{X}$ and $\overline{Y}$ are the means of X and Y, respectively. In multiple linear regression analysis,the coefficient of determination r^2 reflects the explanatory power of the model. A value of $r^2 > 0.70$ suggests that the model can sufficiently explain the data variation. The Durbin-Watson statistic (DW) assesses residual autocorrelation in the regression model; values close to 2 indicate no significant autocorrelation. The F-value analyzes the overall significance of the model, where higher values imply a stronger impact of independent variables on the dependent variable. The P-value reflects the probability of the results, assisting in hypothesis testing. A P-value below 0.05 is considered statistically significant. The data set of this correlation analysis comes from the content of different forms of Na

and Cl in coal and char measured in experiments. Specific data can be found in **Supplementary materials-Experimental Results**.

Neural networks, based on principles of biomimicry, simulated neural connections within the human brain and effectively handle complex relationships and extensive datasets (Muravyev et al., 2021). The most typical neural network consists of several neuron layers: an input layer, multiple hidden layers, and an output layer. Each neuron processes the input from the preceding layer by adjusting weights and applying activation functions, then sends the output to the next layer. Through a large number of training datasets, neural networks continuously refine inter-neuron weights, enabling precise predictions of new data. In this study, inputs included various Na and Cl forms in coal and pyrolysis temperature. This setup allows the neural network to capture intricate factors influencing Na and Cl release. The data used for training and testing the neural network model come from the experiments and measurements conducted in this study. The specific data can be found in **Supplementary materials-Experimental Results**. With the training data, the model accurately forecasts Na and Cl release under varied conditions. This supports the clean and efficient utilization of high-sodium coal in industrial applications.

3. Results and discussion

3.1. Effect of water washing on pyrolysis process

This study initially examined the pyrolysis process differences between SEH and WS for 120 min, followed by a kinetic analysis. 10 mg of both SEH and WS samples were individually weighed and subjected to non-isothermal thermogravimetric experiment under an N_2 atmosphere, with heating rates set at 10 °C•min^{-1}, 20 °C•min^{-1}, 30 °C•min^{-1}, and 40 °C•min^{-1}. Since significant chemical reactions typically do not occur below 200 °C during pyrolysis, rapid mass loss in this range is primarily attributed to moisture evaporation, while the main pyrolysis and reduction reactions usually start above 200 °C (Lin et al., 2014; Guo et al., 2013). In the kinetic analysis, starting at 200 °C also helps reduce instability in thermogravimetric data caused by lower temperatures, ensuring the accuracy of measurements. Therefore, this study selected a temperature range of 200–1200 °C to comprehensively capture the main pyrolysis reactions and calculate corresponding kinetic parameters, including activation energy (E_a) and pre-exponential factor (ln A), to elucidate the pyrolysis mechanisms of these samples.

From the TG curves in Figs. 2 and 3, it is evident that both SEH and WS exhibit smoother weight loss curves at higher heating rates. This can be attributed to the limited heat transfer within the coal, resulting in a pronounced thermal lag effect (Shuang et al., 2010). Therefore, higher temperatures are required to achieve comparable reaction rates during pyrolysis at a higher heating rate. Similarly, the DTG curves for both SEH and WS shift toward higher temperatures, with peak intensities increasing as the heating rate rises. This occurs because higher heating rates lead to a shorter time for the sample to reach its decomposition temperature range (Zhou et al., 2020), causing concentrated reactions that accelerate the breakdown of organic matter and the release of volatiles.

The study utilized the FWO method (Patidar et al., 2022) to examine the linear relationship between ln β and $1/T$ for varying conversion ratios (β: heating rate, T: temperature at a specific conversion ratio). In the low conversion stage, the reaction has not yet fully proceeded and is easily affected by experimental conditions and instability in the initial stage, resulting in large data deviations. Similarly, at the high conversion stage, when the sample is close to complete decomposition and the reaction is approaching completion, the influence of residues and the occurrence of side reactions may affect the activation energy calculation of the reaction. Due to potential data instability in the early and late stages, the analysis focused on the conversion range of 0.2–0.8, which enhances both model applicability and result reliability. The results obtained can be further used to calculate the activation energy E_a and pre-exponential factor ln A at different conversion ratios.

Figs. 2 and 3 reveals that the E_a for both SEH and WS decreases with increasing conversion ratios, demonstrating a dependency of pyrolysis kinetics on conversion. At lower conversion ratios, reactions are dominated by stable organic components (Gao et al., 2024), requiring higher E_a. As the conversion ratio increases, more easily decomposed

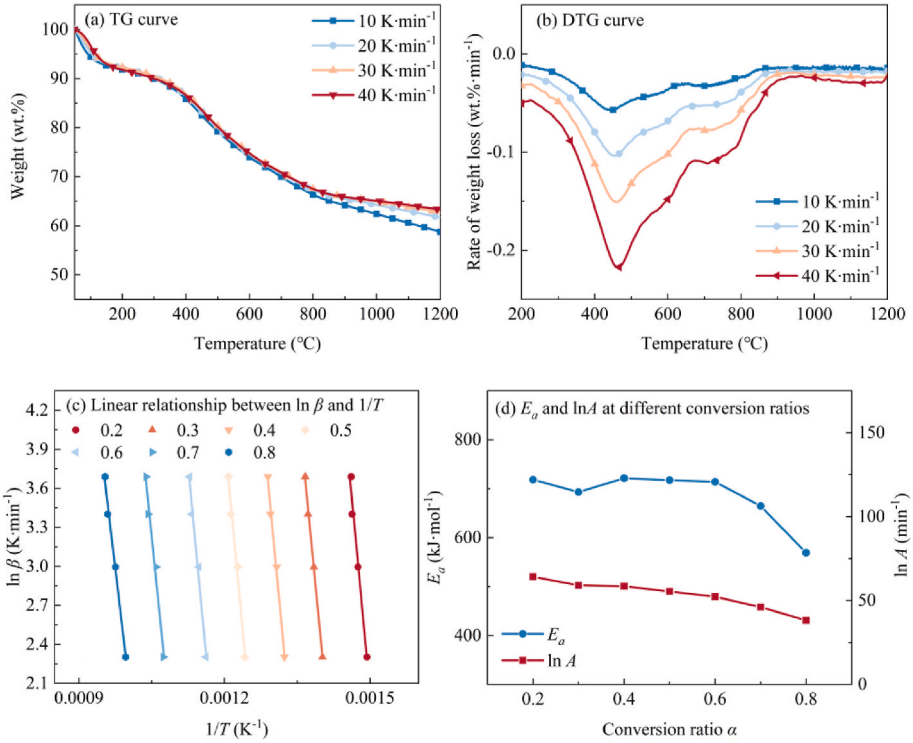

Fig. 2. Thermogravimetric curves at different heating rates and kinetic parameters of water washed coal pyrolysis.

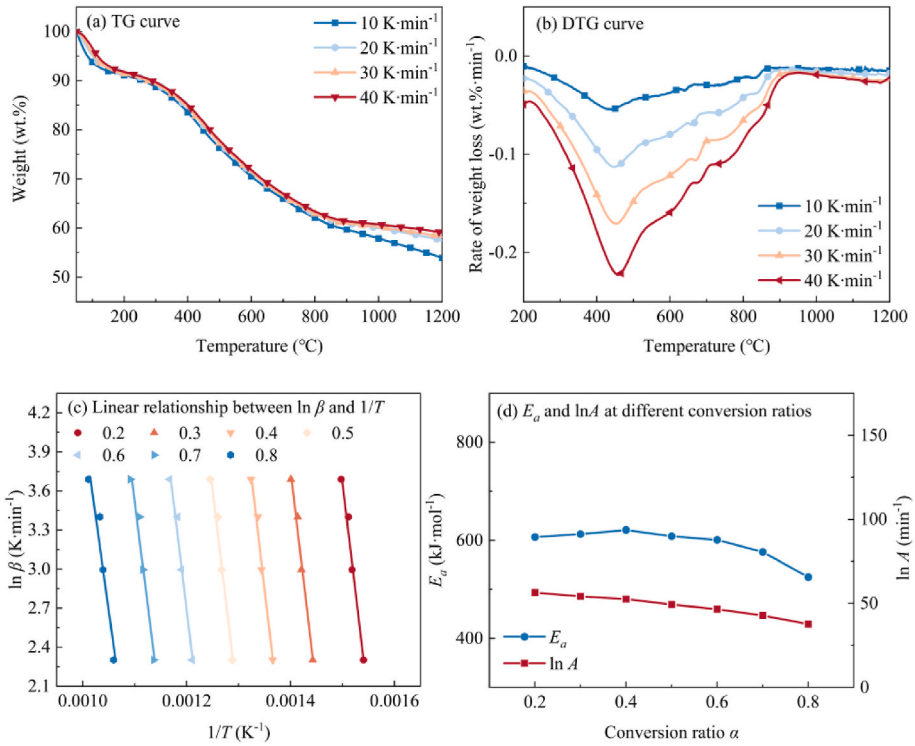

Fig. 3. Thermogravimetric curves at different heating rates and kinetic parameters of raw coal pyrolysis.

components take precedence, reducing the overall E_a. Additionally, intermediate products or free radicals formed during later stages may exert autocatalytic effects (Wu et al., 2023), further lowering E_a.

The E_a and ln A for WS range from 569.10 to 721.35 kJ mol^{-1}, and 38.16–64.19 min^{-1}, respectively, while those for SEH are 524.90–621.10 kJ mol^{-1} and 37.58–56.46 min^{-1}。 The higher E_a for WS likely results from the removal of catalytic minerals during washing, which otherwise lower E_a and enhance reaction rates of SHE pyrolysis. Washing also densifies the coal structure (Wang et al., 2016), increasing stability and reaction difficulty. The higher ln A for WS suggests a greater decomposition probability, allowing more rapid reactions once E_a is achieved. This implies that the removal of minerals facilitates intense decomposition reactions at high temperatures. This may be because the removal of minerals can make the pyrolysis of WS less hindered, resulting in a more intense decomposition reaction at high temperature, ultimately making the WS decompose faster under the same conditions. These differences indicate that alkali metals and minerals significantly influence coal pyrolysis, with SEH and WS potentially following distinct reaction pathways.

Tang et al. (2017) found that Na can accelerate the release of volatiles by catalyzing the cleavage of bridge bonds and inhibiting the condensation of aromatic rings at high temperatures. Zhang et al. (2022a) found that Na can promote the cleavage of fatty side chains (-CH_2-) and the removal of hydroxyl groups (-OH). As the Na content increases, the char yield continues to decrease. Xu et al. (2018b) also found that W-Na will insert into the aromatic ring layer to inhibit graphitization and increase the pyrolysis reaction rate. The previous research conclusions are consistent with the phenomena shown in this thermogravimetric experiment. Na in coal will have a great influence on the pyrolysis process and the release of volatiles.

3.2. Effect of water washing on Na/Cl forms and pyrolysis products

This study investigated the influence of washing time on the contents of various forms of Na and Cl in SEH, determining how different forms were impacted by washing. The pyrolysis of WS in a fluidized bed was followed by product analysis to assess differences due to varying Na and Cl contents.

Fig. 4 (a) and (b) show that SEH has high levels of W-Na and I-Na, with W-Na constituting 68.75 % and I-Na 22.35 %. Washing primarily removes W-Na and some H-Na, while A-Na and I-Na forms are minimally affected. After 120 min of washing, W-Na decreased from 5614 μg g^{-1} to 764 μg g^{-1}, whereas I-Na content only reduced from 1825 μg g^{-1} to 1694 μg g^{-1}. This difference is attributed to W-Na existing as salts that dissolve readily in water, while insoluble forms are bound tightly to minerals in coal (Wang et al., 2015b; He et al., 2023b). Water has limited solubility and can only effectively remove those sodium ions that form weak bonds with inorganic minerals in coal, while insoluble sodium usually requires strong acids or higher temperatures to release (Chen et al., 2020; Wei et al., 2019). The contents of hydrochloric acid-soluble and acetic acid-soluble sodium decreased by 25.45 % and 11.73 %, respectively. This is because hydrochloric acid-soluble and acetic acid-soluble sodium are usually more tightly bound to minerals and organic matter, have stronger chemical bonds, and need to be released under acidic conditions (Guo et al., 2023; Chen et al., 2024). It is worth noting that the content of A-Na in coal increases after 120 min of water washing. This may be due to the existence of multiple chemical reaction balances during the water washing process. Originally, there were some weak acid salt balances related to Na in the coal. As the water washing time increased, the concentrations of hydrogen and hydroxide ions in the system changed, breaking the balance of these weak acid salts. The changes in these ion concentrations will affect the competition of acetate ions and other acid ions for Na, which is beneficial for acetate to bind to Na, thus leading to an increase in the content of A-Na. Moreover, as the water washing time increases, some complex minerals such as aluminosilicates will further dissolve in the water, and the internal Na elements will be released, thereby producing more Na sources that can react with acetate ions, which increases the content of A-Na.

The changes in the content of Cl in different forms in coal are similar to those of Na. In SEH, the content of W-Cl accounts for an extremely high proportion, reaching 95.73 %. W-Cl usually exists in the form of simple inorganic salts, such as sodium chloride or potassium chloride.

These salts are loosely bound in coal and are easily dissolved in water and removed. I-Cl accounts for only 4.27 % of the total Cl content. I-Cl is often tightly combined with organic matter or minerals in coal, forming a complex chemical structure. Water washing is difficult to destroy the chemical bonds of I-Cl in coal. After 120 min of washing, W-Cl decreased from 6280 μg g^{-1} to 698 μg g^{-1}, while the content of I-Cl only decreased from 280 μg g^{-1} to 225 μg g^{-1}.

Therefore, water washing has a great influence on coal quality. Analyzed in combination with Table 1 and Fig. 4, water washing can reduce the ash content (from 6.49 % to 5.59 %). The volatile matter and fixed carbon remain relatively unchanged, which retains the organic matrix to a large extent. The char produced by water-washed coal has a higher ash melting characteristic temperature, which is conducive to the stable operation of high-sodium low-rank coal in the fluidized bed. Water washing also significantly reduces the content of W-Na and W-Cl, greatly reducing the corrosive substances released during pyrolysis,

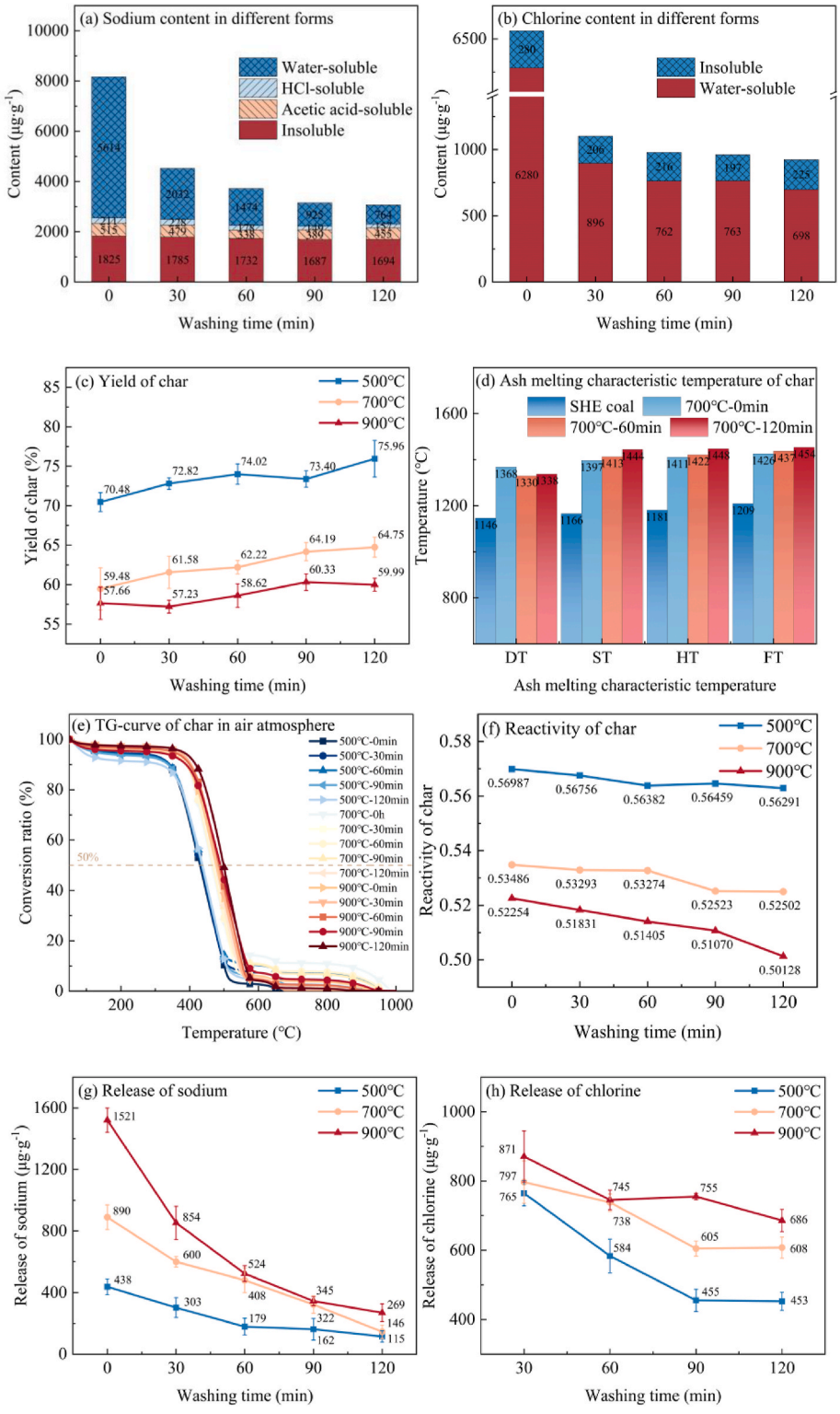

Fig. 4. Characteristics of pyrolysis products produced from coal with different water washing times.

which is conducive to improving the safety and economy of high-sodium coal in the industrial utilization process. The changes in these characteristics provide an important basis for the subsequent discussion of the impact of water washing on pyrolysis products.

Compared with previous studies, Ma et al. (2022) found that the content of W-Cl in coal was significantly reduced after water washing, and the content of Cl in the filtrate was much greater than that of Na. This shows that water washing has a greater impact on Cl than Na. Jiang et al. (2019) found that water washing can significantly reduce the content of W-Na, while I-Na is relatively stable and its content changes little. The conclusions of this study are consistent with the above studies. This shows that water washing can significantly affect the content of W-Na and W-Cl, among which W-Cl is more easily washed out.

Fig. 4 (c) illustrates that the char yield increases with extended water washing time at any pyrolysis temperature, and the increase is more obvious at low temperature. This phenomenon is mainly due to the removal of catalytic alkali metals by water washing. The higher W-Na content (such as NaCl) in unwashed coal can catalyze the decomposition of organic matter and accelerate the release of volatiles (Liu et al., 2025), while such active sites are reduced after water washing, resulting in more organic matter being retained. These observations align with the findings of the thermogravimetric experiments. At higher pyrolysis temperatures, the pyrolysis process is less sensitive to catalysis. At 500 °C, the char yield of SEH is 70.48 %, while that of WS washed for 120 min rises to 75.96 %, with an increase of 5.48 %. At 700 °C, the char yield of SEH is 59.48 %, while that of WS washed for 120 min rises to 64.75 %, with an increase of 5.27 %. At 900 °C, the char yield of SEH is 57.66 %, compared to 59.99 % for WS coal washed for the same duration, with an increase only of 2.33 %. This phenomenon reflects that the catalytic effect weakens at high temperatures and the pyrolysis is dominated by temperature. In addition, the Cl removed during the water washing process will also weaken the destructive effect of Cl on the coal structure, thereby retaining more solid products. These results show that water washing can increase the char yield, especially in low-temperature pyrolysis.

It is worth noting that although the experimental results show a general trend that the longer the water washing time, the higher the char yield. However, the char yield does not necessarily increase with the extension of the water washing time. For example, when the washing time increases from 60 min to 90 min, the char yield at 500 °C decreases slightly. During the long washing process, light organic compounds and low molecular weight substances are leached. These substances would originally promote the formation of char during pyrolysis. In addition, excessive removal of minerals that may contribute to structural stability may also reduce the char yield. Therefore, this phenomenon shows that there is an optimal water washing time. Beyond this time, the benefits of further washing away Na may be offset by these losses. Moreover, since water washing does not have a significant effect on pyrolysis like temperature. It can also be seen from Fig. 4 (c) that the increase in char yield caused by the extension of water washing time does not exceed 5 %. Therefore, the possible errors will cause individual samples to not necessarily show an upward trend. This phenomenon reflects the complex correlation between the water washing process and coal pyrolysis behavior. Moreover, the char yield of the coal washed for 30 min at 900 °C is lower than that of the unwashed coal. This may be because water washing does not significantly affect the char yield. There are certain errors in both measurement and experiment. Therefore, we chose to conduct three parallel experiments and take the average value to determine the results. The yields under the two conditions are close, and in general, the change trend of the char yield at 900 °C is consistent with the change trend at 500 °C and 700 °C.

Fig. 4 (d) further demonstrates that water washing raises the ash melting point of coal. This indicates that water washing effectively removes low-melting-point inorganic compounds, such as water-soluble Na and Cl. By improving the ash melting properties, water washing reduces slagging risks, enhancing the coal's suitability for use in fluidized bed reactors. The reactivity of char produced from WS coal consistently decreases with prolonged water washing, as shown in Fig. 4 (f), regardless of the pyrolysis temperature. At a pyrolysis temperature of 500 °C, the reactivity index of char from SEH is 0.56987, whereas that of char from WS washed for 120 min is 0.56291. Similarly, at 900 °C, the reactivity index of char from SEH is 0.52254, compared to 0.50128 for char from WS washed for the same duration. The reactivity of char pyrolysis from water-washed coal is significantly lower than that of unwashed coal, especially at high temperature. This phenomenon is closely related to the removal of alkali metals and minerals and changes in coal quality. With the removal of catalytic alkali metals (such as Fe and Na), the pyrolysis process tends to form a more ordered carbon structure. Moreover, the removal of minerals destroys the original pore network, and the phenomenon of mineral-induced microfragmentation is also reduced. Therefore, the char is more ordered and graphitized. At higher temperatures, graphitization leads to pore closure. O_2 molecules are difficult to embed between graphite layers, and the contact area with char on the surface is also smaller. Therefore, char pyrolysis from water-washed coal has lower reactivity.

Fig. 4 (g) and (h) show the release of Na and Cl during the pyrolysis of coal subjected to different water washing times. At 500 °C, the Cl release from SEH reached 5163 μg g^{-1}, increasing to 5616 μg g^{-1} at 700 °C and 5934 μg g^{-1} at 900 °C. This demonstrates a clear trend of increasing chlorine release with rising pyrolysis temperatures, with the release ratio increasing from 78.71 % at 500 °C to 90.46 % at 900 °C. Extending water washing time significantly reduced Cl release under identical conditions, primarily due to the removal of W-Cl. For WS washed for 120 min and pyrolyzed at 700 °C, chlorine release decreased to 608 μg g^{-1}, representing a reduction of 5009 μg g^{-1}, compared to SHE. When the washing time was extended from 30 min to 120 min, the Cl release decreased by 185 μg g^{-1} at 900 °C and by 312 μg g^{-1} at 500 °C. I-Cl combined with organic chlorine or minerals has better thermal stability at lower pyrolysis temperatures and will not volatilize easily. Since the release of Cl is less affected by the conversion relationship between different forms of Cl at higher temperatures, it is more controlled by temperature. Some W-Cl recombined with inorganic components to form non-volatile chlorides will begin to decompose at higher temperatures, further increasing the Cl release. Therefore, at 900 °C, the decrease in Cl release is relatively smaller with the extension of washing time.

A similar trend was observed for Na release. At 500 °C, the Na release from SEH was 438 μg g^{-1}, which dropped to 115 μg g^{-1} for WS washed for 120 min. This reduction is attributed to the removal of W-Na, which is readily released during pyrolysis. At 900 °C, sodium release from SEH was 1521 μg g^{-1}, while WS washed for 120 min reduced this to 269 μg g^{-1}. These findings indicate that water washing effectively minimizes the release of Na and Cl during pyrolysis, mitigating contamination and corrosion issues during the high-temperature utilization of high-sodium coal.

Although washing is expected to reduce the total release by removing soluble salts, a more detailed comparison reveals temperature-specific behavior. At low temperature (500 °C), the Na release is significantly reduced due to the efficient removal of W-Na, which is consistent with the report of Xu et al. (2018a) that "W-Na is the main source of low-temperature release". At medium temperature (700 °C), the decomposition of H-Na and A-Na leads to a small increase in release, but the increase in washed coal is lower than that of unwashed coal due to the densification of the residual structure, which is consistent with the conclusion of Chen et al. (2020) that "medium-temperature release is controlled by the content of decomposable Na forms". At high temperature (900 °C), mineral melting in SEH promotes a large release of Na and Cl, while the release of washed coal is smaller due to the lattice stability of I-Na, which is consistent with the finding of Wang et al. (2015b) that "High-melting-point Na compounds are released at higher temperatures". It is noteworthy that Cl release tends to be flat at high temperatures, because the W-Cl remaining after water washing has been

almost completely removed, while the chemical stability of I-Cl inhibits further release. These results show that water washing pretreatment has a differential regulatory effect on the release of Na and Cl at different temperatures. The change of residual Na and Cl forms is still the key factor in their final release behavior.

In Fig. 4 (g), the amount of Na released during the pyrolysis of coal washed for 60 min and 90 min at 700 °C and 900 °C is relatively close. This may be because the intensity of the pyrolysis reaction itself at higher temperatures masks the effect of slight differences in coal samples on Na release. The higher the temperature, the greater the decrease in the amount of Na released with the increase in water washing time. In addition, since a large amount of W-Na is washed away, the Na release may have been reduced to a certain lower level. Meanwhile, the amount of I-Na removed during the water washing process is less and relatively stable at higher pyrolysis temperatures. Therefore, this phenomenon occurs at 700 °C and 900 °C.

3.3. Effect of water washing on char characteristics

Char produced from pyrolysis of different coal sample was analyzed using Raman and XRD techniques, with results shown in Fig. 5. With increasing washing time across various pyrolysis temperatures, the ratios of $I_{(Gr+VL+Vr)}/I_D$, I_G/I_D, I_G/I_{total}, and I_S/I_G in char exhibit consistent trends. These changes may arise from variations in Na and Cl content and from the impact of water washing on coal properties.

The increase in $I_{(Gr+VL+Vr)}/I_D$ with washing time indicates reduced structural disorder in char derived from washed coal samples. This is primarily due to the removal of water-soluble Na and Cl, which disrupt the carbon structure during pyrolysis, introducing disorder (Zhang et al., 2022a). The removal of Na and Cl impurities during washing allows for easier rearrangement of carbon atoms during pyrolysis, thereby enhancing the structural ordering and reducing carbon defects. Furthermore, moisture variations influence the aromatic structure in char (Butuzova et al., 1998). Table 1 shows that washing reduces the moisture content of coal. This phenomenon accounts for the lower reactivity of char from pyrolysis of WS compared to SEH under identical conditions.

The I_G/I_D also increases with washing time, suggesting a rise in the content of ordered carbon and a greater degree of graphitization in the char. During the washing process, water molecules may interact with active sites on char surfaces, hydrolyzing or restructuring functional groups like hydroxyl and carboxyl groups (Zhao et al., 2024). Consequently, the carbon structure of char produced by WS pyrolysis tends to form orderly aromatic layers, as the well-rearranged carbon layers contribute to reduced disordered structures.

The slight increase of I_G/I_{total} indicates an increase in the proportion of graphite-like structures within char. Additionally, washing removes certain internal moisture, reducing the likelihood of small-molecule side reactions during pyrolysis. The presence of water typically promotes these side reactions at high temperatures, introducing more defect structures (Hosokai et al., 2016; Wang et al., 2024a). By altering factors that affect graphite formation in the carbon structure, washing enhances the stability and graphitization of the char produced post-pyrolysis.

The I_S/I_G decreases with extended washing, likely because water facilitates conformational adjustments and chain rearrangement of carbon structures. The aliphatic structures present within the pores of coal are likely to undergo redistribution during water washing (Meng et al., 2023). The aliphatic carbon that was initially randomly dispersed within the pores may relocate either outside the pores or to more stable positions under the combined influence of the water washing force and the interaction between water and carbon. During this process, the stacking pattern of the aliphatic structure is subject to alteration, giving rise to the formation of more ordered aromatic structures and resulting in a decrease of I_S/I_G.

As shown in Fig. 5, XRD analysis of char indicates that d_{002} decreases with rising temperature, indicating a reduction in carbon interlayer spacing. At higher temperatures, volatiles and other impurities are gradually released (Zhang et al., 2022b). Char can more easily obtain energy to overcome the interaction forces between molecules, making the arrangement of the carbon layer more orderly. This leads to denser stacking, reduced interlayer spacing, and increased char density. As the pyrolysis temperature increased, the value of L_c, which represents the stacking height of carbon microcrystals, gradually decreased. This reduction can be attributed to structural reorganization and bond-breaking reactions within the coal matrix. At elevated temperatures, weaker bonds, such as C-C bonds or those near heteroatoms like oxygen and nitrogen, become more susceptible to cleavage due to thermal energy (Nagaraja et al., 2021; Hao et al., 2025). This cracking may cause the carbon layers originally stacked along the c-axis to be partially destroyed, thereby reducing the height of the graphite crystallites. Conversely, L_a increases with increasing temperature. Higher pyrolysis temperature promotes the carbonization reaction, resulting in the gradual removal of disordered structures (such as heteroatoms and defects) in the char and the formation of a more regular graphitized structure (Li et al., 2017a). Meanwhile, more violent chemical reactions and structural rearrangements at high temperatures will cause the covalent bonds between carbon atoms to reform, thereby forming larger aromatic hydrocarbon structures. This structural reorganization helps the carbon layer to extend laterally.

Fig. 5 also illustrates that d_{002} decreases at all temperatures with longer washing times. Washing removes minerals and inorganic impurities that otherwise separate carbon layers, thus reducing interlayer spacing during pyrolysis. Additionally, hydrolysis and dissolution of functional groups on the coal surface lower electrostatic repulsion between carbon layers, further contributing to the reduction in d_{002}. The removal of minerals served as active centers during pyrolysis, such as iron and calcium, may restrict microcrystal growth, leading to a decrease in L_c (Yao et al., 2024; Ding and Zhang, 2017). Prolonged washing may also damage the initial structure of coal, breaking macromolecular bonds and further limiting microcrystal formation. An increase in pyrolysis temperature also leads to a reduction in the L_a value. This phenomenon arises from similar mechanisms that influence L_c. During water washing and subsequent pyrolysis, the originally stable microcrystalline structure undergoes reorganization. The formation of a new structure constrains the lateral growth of microcrystals, thereby reducing L_a. The findings from the XRD analysis of char align with the previously discussed reactivity trends. As the temperature increases and washing time extends, the internal structural order of char improves, thereby reducing its reactivity.

Fig. 6 presents the FTIR spectra of char obtained from pyrolysis of WS with different washing times across varying pyrolysis temperatures. According to the Beer-Lambert law (Zhang et al., 2017b; Lin and Ritz, 1993), the intensity or area of absorption peaks in FTIR spectra is directly proportional to the concentration of specific components within the sample. Based on Li et al. (2019), the bands between 3600 and 3000 cm^{-1} are primarily attributed to the stretching vibrations of hydroxyl (-OH) groups, while the 1800-1300 cm^{-1} region corresponds to oxygen-containing functional groups such as carboxyl (-COOH) and carbonyl (C=O). The 1300-1000 cm^{-1} range represents the absorption peaks of ether (both aliphatic C-O-C and aromatic R-O-R), and the 900-700 cm^{-1} range is mainly associated with aromatic C-H groups.

As shown in Fig. 6, increasing the pyrolysis temperature from 500 °C to 900 °C led to a continuous decrease in the intensity of characteristic peaks within the 1800-700 cm^{-1} region. This decline is due to enhanced structural rearrangement and aromatization at higher temperatures, as the carbon matrix transitions to a more stable aromatic structure. Consequently, non-aromatic functional groups such as -COC-, -COOH, and C=O are broken down, releasing volatile compounds such as CO、CO_2. The high intensity of the -OH absorption band in the 3600-3000 cm^{-1} region suggests that hydroxyl groups, which possess high bond energies, remain largely intact at low pyrolysis temperatures (Wang et al., 2024b). As the temperature increases, the intensity of this peak

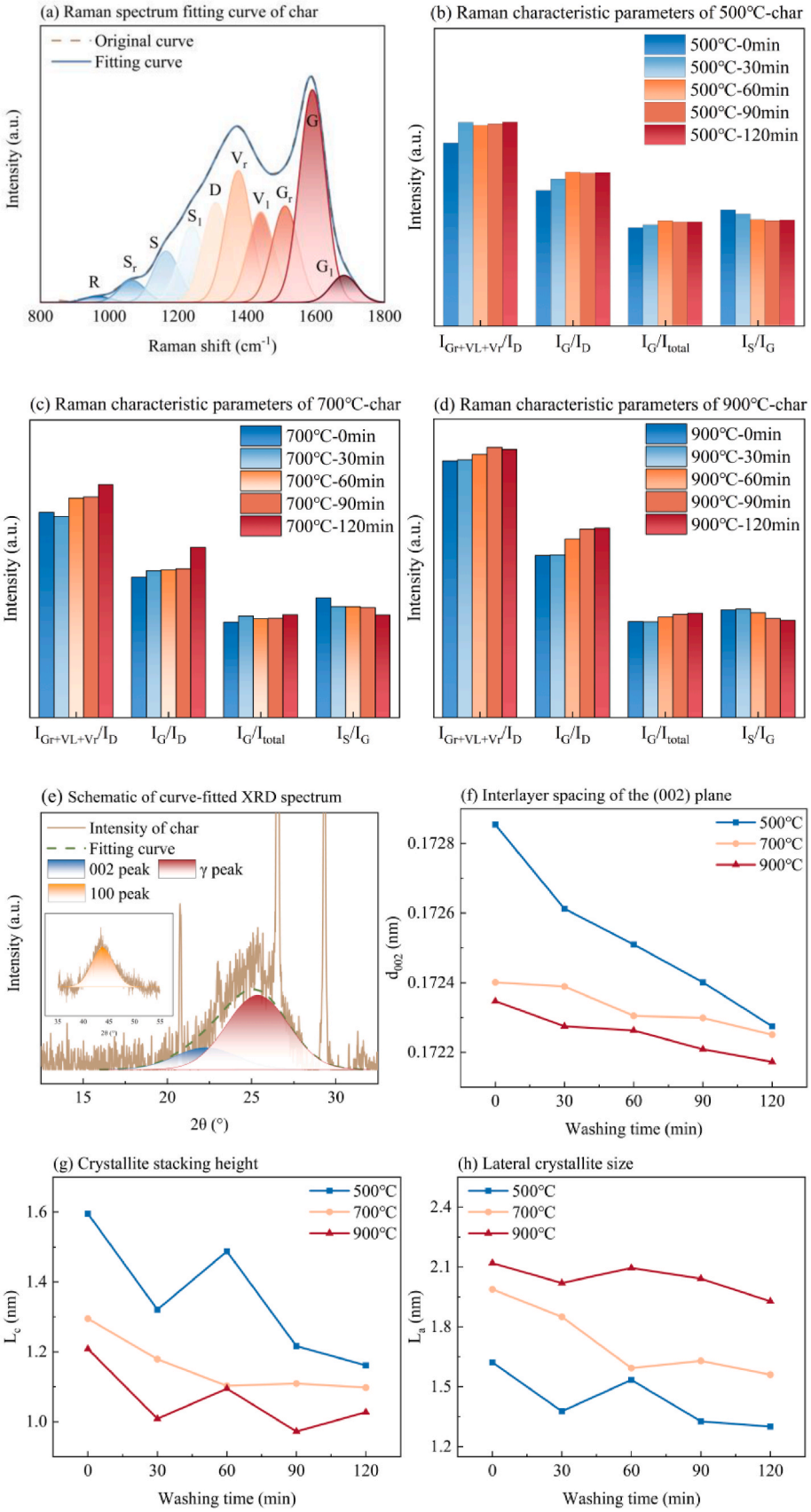

Fig. 5. Microstructural characteristics of char produced from coal with different water washing times.

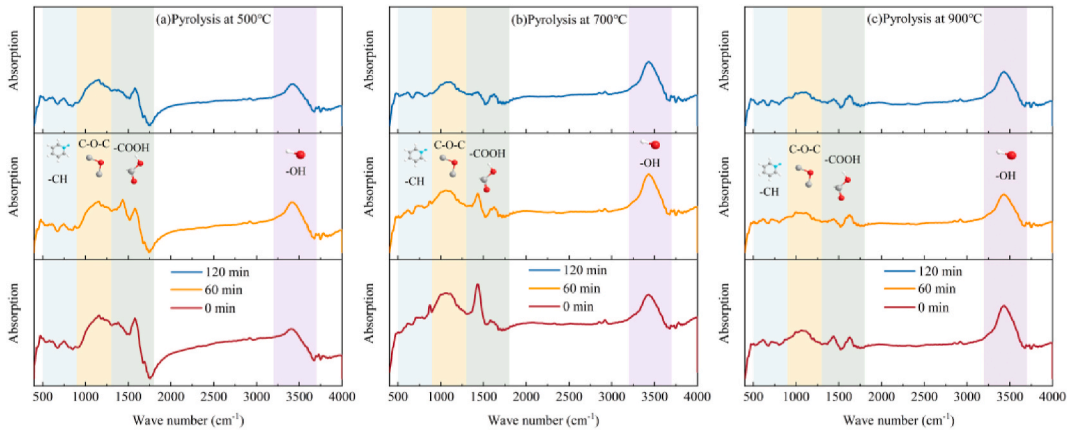

Fig. 6. The fitted curve of FTIR spectrum for char produced by SEH with different wash time at different temperature.

first rises slightly, then decreases. This initial increase may result from the decomposition of water and certain oxygen-containing groups (such as -COOH) that generate -OH. At higher temperatures, even stable bonds like ether linkages (-COC-) begin to break, forming additional -OH groups. However, further temperature increases promote polycondensation and -OH decomposition, reducing the -OH peak intensity.

Washing coal reduces soluble oxygen-containing groups, such as -COOH and -OH, as these hydrophilic groups can be easily dissolved and removed (Ju et al., 2022). Prolonged washing further diminishes the presence of these groups. Additionally, washing removes volatile components, minerals, and catalytic substances. This will result in a more stable structure of the char produced by pyrolysis and reduce the number of active functional groups in the char after pyrolysis. Therefore, the FTIR spectra of char produced by WS with extended washing exhibit weaker characteristic peaks.

Fig. 7 displays the adsorption-desorption curves and pore size distributions of chars prepared under different conditions. As pyrolysis temperature rises, the adsorption capacity (P/P_0) of chars produced by both SEH and WS increases. At low pressures, the adsorption and desorption curves do not coincide but overlap at higher pressures, forming a hysteresis loop. Based on the classification of the adsorption-desorption curves (Sing et al., 1985), the isotherms follow a type II adsorption behavior, indicating a complex pore structure in the char. As pressure increases in the initial range (P/P_0 = 0–0.8), adsorption rises gradually with a convex manner of curve, suggesting that gas fills mesopores progressively. However, due to the limited presence of macropores, the increase remains gradual. At higher pressures (P/P_0 = 0.8–1.0), a sharp rise in adsorption is observed, indicative of capillary condensation within macropores (Gregg and Sing, 1982), as gas molecules fill larger pores.

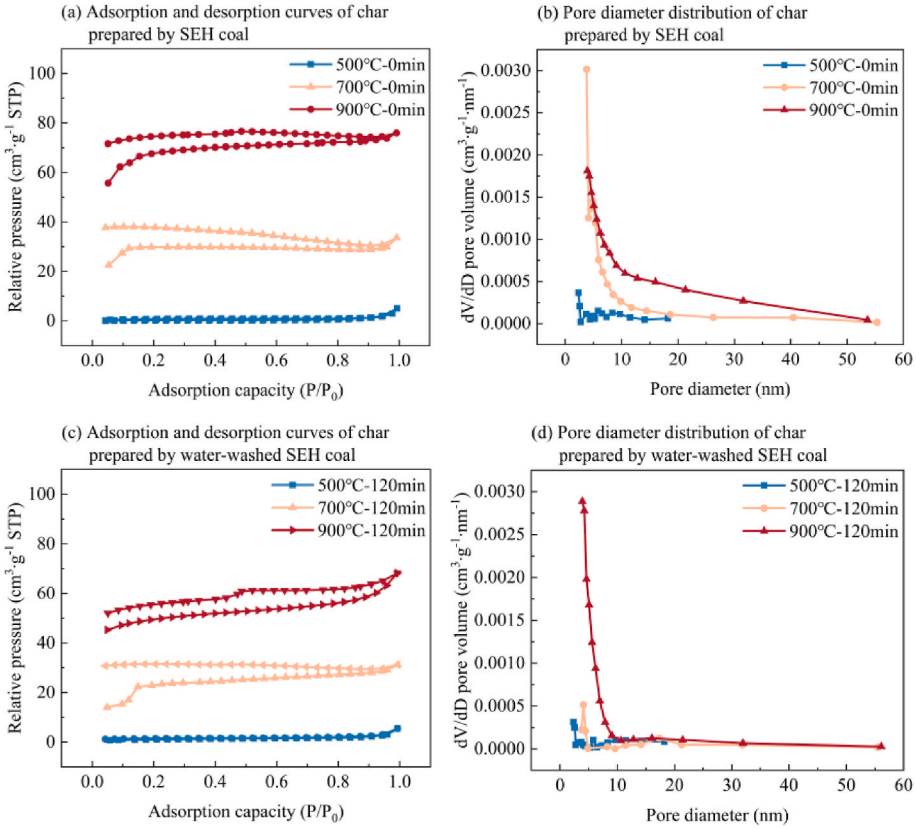

Fig. 7. Adsorption-desorption curves and pore distribution of char prepared under different conditions.

The pore size distribution changed significantly with temperature. At 500 °C, pore sizes are concentrated in a narrow range with low peak values due to limited decomposition and volatile release (Zhang et al., 2022b). At 700 °C, higher temperatures accelerate organic decomposition, with more volatiles escaping and leaving more and larger pores (Ju et al., 2022). Consequently, the curve peak of pore size distribution rises, and the quantity of macropores and mesopores increases. At 900 °C, the macromolecular structure in coal is more thoroughly decomposed. High temperature promotes the expansion of pores and the interconnection of micro-channels (Meng et al., 2023), leading to the generation of more macropores. For chars produced by WS, similar temperature-driven changes in pore distribution occur, as shown in Table 4, where higher temperatures facilitate the formation of additional pore structures, especially micropores and mesopores, thereby increasing specific surface area.

Comparing adsorption-desorption curves, chars from WS exhibit lower adsorption capacity than those from SEH under the same conditions. This may result from mineral decomposition or phase changes in SEH during pyrolysis, which can generate or enlarge pores (Zhang et al., 2022b). Washing removes such minerals, resulting in less new pores post-pyrolysis and lower adsorption capacity. Additionally, washing eliminates the alkali metals that enhance chemical activity on char surfaces during pyrolysis, further lowering adsorption for chars from WS. This is confirmed in Table 4, which shows that chars from WS possess smaller specific surface areas. Specific surface area is a key factor influencing adsorption. Lower surface area typically corresponds to lower adsorption capacity (Gritti and Guiochon, 2007).

Fig. 7 and Table 4 also illustrate that, at identical pyrolysis temperatures, chars from WS exhibit distinct pore characteristics compared to those from SEH. The pore size distribution in WS char is narrower, and the increase in mesopores and macropores at 700 °C and 900 °C is smaller compared to SHE char. This difference likely stems from the removal of minerals and alkali metals during washing, which alters surface chemistry and initial structure, potentially stabilizing the organic matrix and reducing microstructural rearrangement and fracture during pyrolysis. Consequently, the formation of large pores is limited, and pore expansion is constrained.

In addition to the influence of changes in minerals and coal quality after water washing on the char structure, the initial Na and Cl content in the coal may also have an effect on the char structure. Na and Cl in coal can increase the reactive sites through the mechanisms of sodium catalyzed oxygen transfer (Han et al., 2022) and chlorine activated free radicals (Ma et al., 2025). Na and Cl, especially in the form of salts, may contribute to the formation of pores during devolatilization and high-temperature volatilization. Compared with SEH, the pore-forming ability of Na and Cl can only be compensated by the decomposition of organic matter and the interconnection of macropores due to the absence of minerals (Li et al., 2017b) during WS pyrolysis. Therefore, the pore development of char produced by SEH pyrolysis is better than WS.

Compared with previous studies, Wei et al. (2022) through FTIR analysis found that more aromatic functional groups were produced after water washing, and the aromatization effect was enhanced. Therefore, this is consistent with the conclusion of this study that the content of -OH and -COOH groups in char is reduced. Bao et al. (2023) found that pyrolysis temperature has a strong control effect on the structure of char, and a higher alkali metal content will destroy the carbon structure, thereby increasing the char reactivity. This conclusion can well support the conclusions of this study. After water washing to remove alkali metals, the catalytic effect of Na is weakened, and the char tends to be more graphitized and ordered. Barszcz et al. (2024) found that pyrolysis temperature can significantly change the char structure. They also found that the melting and recrystallization of alkali metal halides at high temperatures will lead to the formation of different crystal structures in char, resulting in more micropores and increasing the specific surface area of char. This is consistent with the conclusion of this study that the pores and specific surface area of char produced after washing are reduced.

The mechanism diagram of the effects of water washing and Na content on the characteristics of pyrolysis products is shown in Fig. 8.

Table 4
Surface properties of chars prepared under different conditions.

Temperature (°C)	Wash time (min)	Specific surface area (m^2/g)	Micropore specific surface area (m^2/g)	Total pore volume (cm^3/g)	Micropore volume (cm^3/g)
500	0	3.1275	2.1085	0.0076	0.0008
500	120	2.7046	1.7308	0.0068	0.0007
700	0	110.3015	109.4954	0.0506	0.0483
700	120	91.0757	80.8799	0.0446	0.0323
900	0	230.4757	222.4439	0.1136	0.1040
900	120	165.3872	150.3956	0.0970	0.0718

3.4. Related factors and prediction of Na and Cl release

3.4.1. Correlation analysis and data sources

Previous research has shown that the release of Na and Cl during the pyrolysis of high-sodium coal is correlated with their different forms (Liu et al., 2018c; Yang et al., 2018; Guo et al., 2017b). The content of W-Na, hydrochloric acid-soluble sodium, acetic acid-soluble sodium, insoluble sodium, W-Cl, and insoluble chlorine each has an impact on the release of Na and Cl during pyrolysis. Additionally, as indicated by the above analysis, changes in pyrolysis temperature also significantly affect Na and Cl release (Wang et al., 2015b). This study employed correlation analysis to assess the relationships and correlation strength between the Na and Cl release and the seven aforementioned variables during pyrolysis. To enhance accuracy, the study conducted extensive experiments, measuring the content of various Na and Cl forms in coal samples washed at intervals of 10 min for a total of 0–120 min. Each sample was pyrolyzed at different temperatures, and the release ratios of Na and Cl were measured. Experimental data are summarized in **Supplementary materials - Experimental Results**.

In this study, multiple linear regression was used as a preliminary exploratory tool to identify and quantify the effects of different forms of Na and Cl on their release during pyrolysis. Although the effects of pyrolysis may be nonlinear in nature, linear regression provides an intuitive way to explain the significance, directionality, and correlation strength of variables. These results are not used for final predictions. Before constructing the nonlinear neural network prediction model introduced later in this article, the conclusions of multiple linear regression are mainly to understand the key characteristics and influence trends. For the actual research purpose, the multiple linear regression model is relatively simple and intuitive. In addition, by calculating indicators such as correlation coefficient, determination coefficient, and Durbin-Watson statistic, the goodness of fit and reliability of the results can be effectively evaluated. If nonlinear regression is used, under the sample data volume of this study, overfitting may occur, which will reduce the predictive ability and generalization of the model. Therefore, after comprehensive consideration, this study chose multiple linear regression as the analysis method.

3.4.2. Multivariate regression analysis

Multivariate regression analysis was applied to these results, summarized in Tables 5 and 6. In Table 5, linear correlation coefficients between Na release and other factors shift with temperature. This indicates that the pyrolysis temperature has an important influence on the release of Na. *P*-values below 0.05 indicate that selected variables have a statistically significant impact on Na release. *Durbin-Watson* values around 2 across temperatures suggest no significant residual autocorrelation, with evenly distributed residuals and strong model fit (Durbin and Watson, 1992). A potential limitation of regression analysis is the

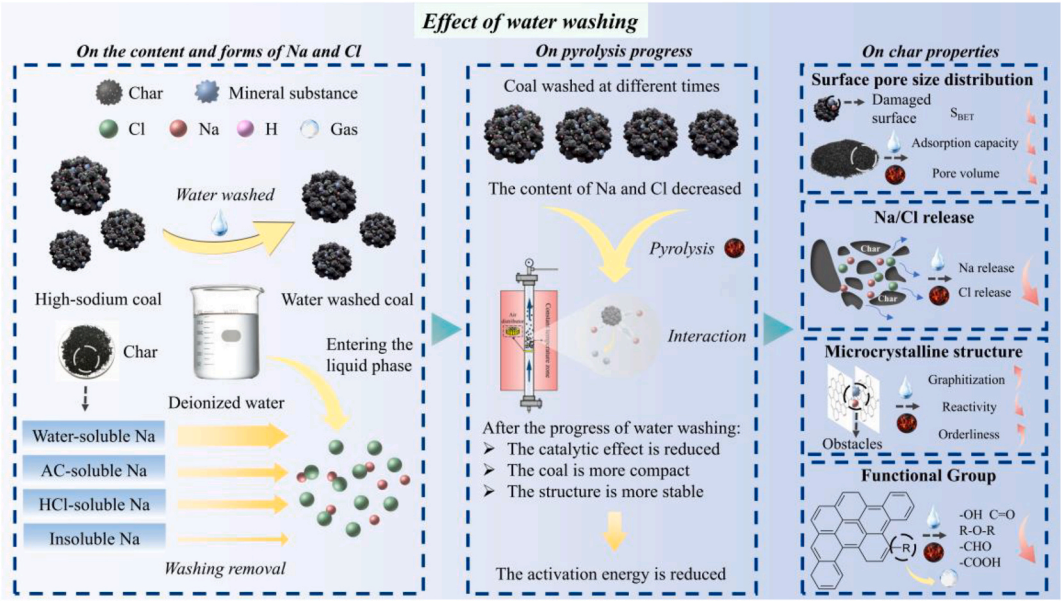

Fig. 8. Mechanism diagram of the effects of water washing and Na content on the characteristics of pyrolysis products.

Table 5
Multiple linear regression analysis characteristic parameters of Na release.

Pyrolysis temperature	Characteristic parameters					
	Model Summary					
	r	r^2	*degree of freedom*	*Durbin-Watson*	*F*	*P*
500 °C	0.908	0.825	6	2.193	4.721	0.040
700 °C	0.926	0.713	6	2.207	5.980	0.023
900 °C	0.963	0.855	6	1.964	12.794	0.003
	Standardized coefficient					
	W-Na	H-Na	C-Na	I-Na	W-Cl	I-Cl
500 °C	1.060	0.262	0.023	−0.199	−0.551	0.219
700 °C	1.606	0.128	−0.206	−0.068	−0.761	−0.077
900 °C	1.493	0.199	−0.089	−0.522	−0.606	0.236

Table 6
Multiple linear regression analysis characteristic parameters of Cl release.

Pyrolysis temperature	Characteristic parameters					
	Model Summary					
	r	r^2	*degree of freedom*	*Durbin-Watson*	*F*	*P*
500 °C	0.999	0.998	6	1.978	1315.005	0.001
700 °C	0.999	0.996	6	2.030	559.376	0.001
900 °C	0.999	0.999	6	2.229	1490.886	0.001
	Standardized coefficient					
	W-Na	H-Na	C-Na	I-Na	W-Cl	I-Cl
500 °C	0.153	0.011	−0.020	−0.016	0.891	−0.013
700 °C	0.097	0.016	−0.012	0.033	0.946	−0.073
900 °C	0.058	0.022	−0.016	−0.041	0.976	−0.022

multicollinearity between predictor variables. Since different forms of Na and Cl originate from the same coal sample and may be interconverted during pyrolysis, they may be correlated to some extent. Although the regression model showed a good overall fit (high r^2 and low *P* value), the presence of multicollinearity may affect the interpretability of the effects of individual predictors. In order to quantitatively assess the potential multicollinearity between the predictor variables used in the regression model, the variance inflation factor (VIF) of each input variable was calculated and summarized in Table 7. Generally, VIF values less than 10 indicate that the model is well constructed and less affected by multicollinearity. The results show that all VIF values are less than 10, which indicates that although there is a certain correlation between different forms of Na and Cl, there is no serious multicollinearity among all variables. Therefore, the regression model constructed in this study and the conclusions obtained are statistically reliable.

The high r^2-values also reveal a strong correlation between Na release and Na, Cl forms. At 500 °C, the *F*-value is 4.721, with a *P*-value of 0.034. When the pyrolysis temperature increases to 700 °C, the *F*-value rises to 5.980, and the *P*-value decreases to 0.023. This indicates that at lower temperatures, the release of Na is limited, and the influence of the variables is not fully manifested, resulting in a less significant model fit. As the temperature increases, the significance level of the model improves. At 900 °C, the *F*-value further increases to 6.706, while the *P*-value decreases to 0.014. At this temperature, most Na and Cl components have been released and decomposed, strengthening the correlation between their release and the influencing variables, thereby enhancing fitting effect of the model.

The standardized coefficients from regression analysis show that W-Na has the strongest positive correlation with Na release at pyrolysis temperatures of 500 °C, 700 °C, and 900 °C, especially pronounced at higher temperatures. This finding aligns with previous results indicating that W-Na is the primary contributor to Na release during pyrolysis (Li et al., 2017b). The standardized coefficient for insoluble sodium is negative across all pyrolysis temperatures. Existing studies suggest that W-Na reacts with mineral components in coal at high temperatures, transforming into insoluble sodium (Zhang et al., 2020; Tian et al., 2025), which means that insoluble sodium undergoes limited volatilization or transformation at high temperatures. Additionally, insoluble sodium will form local deposits in the pores or on the surface of coal at high temperature, which will block the diffusion channels and hinder the release of sodium. The influence of water-soluble and insoluble chlorine on Na release varies with temperature. Compared to insoluble chlorine, W-Cl has a greater effect on Na release, likely due to chlorine adsorption and deposition on coal pores (Ge et al., 2019), which

Table 7
VIF values of different Na and Cl forms in regression analysis.

	W-Na	H-Na	C-Na	I-Na	W-Cl	I-Cl
VIF values	6.490	2.157	1.801	3.250	6.812	3.331

obstructs Na diffusion channels or interacts with Na during diffusion, slowing Na release. The presence of W-Cl may also alter the bonding state of Na within the coal structure by interacting electrostatically or chemically with nearby atoms or functional groups (Zhang et al., 2021), stabilizing Na in localized regions of the coal.

Table 6 further indicates a high degree of linear correlation between Cl release and selected variables, regardless of pyrolysis temperature, with r^2-values of 0.998 at 500 °C, 0.997 at 700 °C, and 0.999 at 900 °C. The high r^2-value shows an excellent model fit. *Durbin-Watson* values are 1.978 at 500 °C, 2.030 at 700 °C, and 2.229 at 900 °C, all close to 2. This shows that the residual sequence of the regression model has no significant autocorrelation and the model fits well. The consistently low *P*-values across temperatures indicate that the overall model is statistically significant. The higher *F*-value at 500 °C may be attributed to the significant impact of both water-soluble and insoluble chlorine on Cl release, increasing the explanatory power of the regression model. As temperature increases to 700 °C, the *F*-value declines slightly, which may be due to the polycondensation reactions during pyrolysis. The polycondensation reactions that occur during coal pyrolysis at 700 °C (Wang et al., 2020; Jüntgen, 1984) may affect the release of different forms of Na and Cl. At this temperature, most W-Cl has been fully released, while insoluble chlorine has yet to completely decompose, creating more complex interdependencies between factors and reducing overall explanatory power of the model. At 900 °C, Na and Cl release from all forms and pyrolysis reactions reach completion. Consequently, the variables affecting Cl release exhibit their strongest influence, as reflected by the higher *F*-value.

It is worth noting that in Table 5, the standardized regression coefficients of C-Na and I-Cl that affect Na release have different directions of action at different pyrolysis temperatures. At low temperatures, the complex structure formed by some C-Na and organic matter or weakly polar minerals is in a relatively loose binding state. Therefore, C-Na can be used as a potential source of Na release, and its regression coefficient is positive. As the temperature increases, the pyrolysis reaction becomes more intense, the reaction and structural reconstruction between minerals intensify, and the C-Na is more likely to undergo mineralization reactions with elements such as Al and Si in char and be converted into non-volatile mineral-bound Na. Therefore, the presence of C-Na at high temperatures actually reduces the amount of Na released, and its regression coefficient is negative. For I-Cl, at lower pyrolysis temperatures, the weaker organic chlorine bonds in the structure have begun to crack, and combined with Na to escape the reaction system, promoting the Na release. At 700 °C, the pyrolysis process enters the active stage of condensation reaction, and many chlorines are reconstructed to form more stable aromatic chlorinated structures or converted into non-volatile chlorinated minerals, making it more difficult to combine with Na. At 900 °C, the high temperature causes the originally stable aromatic chlorine bonds and some Cl-minerals to break, reacting with the Na in the system to generate a NaCl escape reaction system, thus showing a positive effect again.

Additionally, the changes in the magnitude of standardized coefficients with increasing pyrolysis temperature can be attributed to the evolving thermochemical behavior of Na and Cl species. W-Na exhibits a stronger positive influence at higher temperatures due to its increased volatility and greater likelihood of being released in gaseous form. After the temperature is increased from 500 °C to 700 °C, H-Na may form more thermally stable compounds or participate in secondary reactions with other minerals, which could reduce their apparent contribution to release. When the temperature is higher, chemical bonds of H-Na gradually break and participate in the Na release. At high temperatures, I-Na tends to form local deposits in the pores or on the surface of char, blocking the diffusion channels of Na and hindering the Na release. At lower temperatures, the hindering effect of I-Na is relatively weak, so the absolute value of its standardized coefficient will change. These temperature-dependent mechanisms alter the relative dominance of each variable, thereby affecting their regression coefficients.

The standardized coefficients further reveal that W-Cl consistently has the highest impact on Cl release, with its influence intensifying at higher temperatures. This implies that W-Cl is a primary contributor to Cl release, with ease of desorption at lower temperatures and accelerated volatilization at elevated temperatures. W-Na also positively correlates with Cl release, with its influence strongest during low-temperature pyrolysis. In these conditions, W-Na may react with other components in the coal matrix (Ge et al., 2019), promoting Cl release. The negative standardized coefficients for insoluble chlorine at all temperatures suggest that it may restrict Cl release due to its structural stability within the coal, even at high temperatures.

According to previous studies, Zhou et al. (2025) found that correlation analysis showed good results in studying coal pyrolysis. Zhao et al. (2017) found that the chemical forms of Na and Cl affect their release during pyrolysis. Cl tends to be released more easily, while Na may be retained in the form of minerals or organic sodium. This is consistent with our correlation study results.

3.4.3. Neural network modeling

Although laboratory experiments can provide insights into reaction mechanisms and corresponding data, they are often time-consuming and labor-intensive. In addition, in actual industrial operations, multiple interacting factors (such as different chemical forms of Na and Cl, structural properties of coal, and operating temperature) make empirical correlations established using traditional regression methods inaccurate. Neural network models have significant advantages for such complex relationships. They are able to learn hidden information from data and generalize predictions to unknown conditions. By combining experimental data with neural network modeling, this study provides a more efficient and scalable method for predicting Na and Cl release. This method aims to provide a data-driven prediction tool for Na and Cl release for the industrial production of high-sodium low-rank coal, providing a basis for the intelligent control of pyrolysis processes.

The multiple linear regression analysis demonstrated that each of the seven selected factors has a certain influence on Na and Cl release. To address the difficulty of calculating and predicting the release ratio of Na and Cl during industrial high-sodium coal utilization, this study developed a neural network model to predict Na and Cl release, aiming to realize intelligent control of high sodium coal industrial application and optimize the pyrolysis process. The neural network architecture is illustrated in Fig. 9 (a). The model code is available in the **Supplementary materials - Neural network model code**.

Using data from the **Supplementary materials - Experimental Results**, 40 data sets were randomly selected as training data, while an additional 5 sets served as test data to evaluate the predictive capability of the model. The selection of hidden layers and node numbers was guided by the complexity of the problem, data quantity, and available computational resources. In this study, due to the multiple variables, a neural network with a minimum of four hidden layers was initially constructed to enhance prediction accuracy. The trial-and-error method was used to determine the optimal node configuration within the hidden layers, with the training error results presented in Fig. 9 (b). As shown, the prediction error for Na release is minimized at 26 nodes, while Cl release predictions achieve the smallest error with 24 nodes. Based on these results, Fig. 9 (c) indicates that both Na and Cl predictions reach the lowest error level with a four-hidden-layer model structure, suggesting that fewer hidden layers help avoid overfitting while ensuring prediction accuracy. As the dataset in this study was relatively small, an excessive number of hidden layers may lead to overfitting, making it difficult to apply to the test data. Thus, the final model configurations for Na and Cl release prediction include four hidden layers with 26 and 24 nodes, respectively. The corresponding prediction results are shown in Fig. 9(d) and (e).

Due to the potential influence of the number of nodes on the prediction accuracy of the model, a single evaluation is insufficient to demonstrate the stable performance of the model. To comprehensively

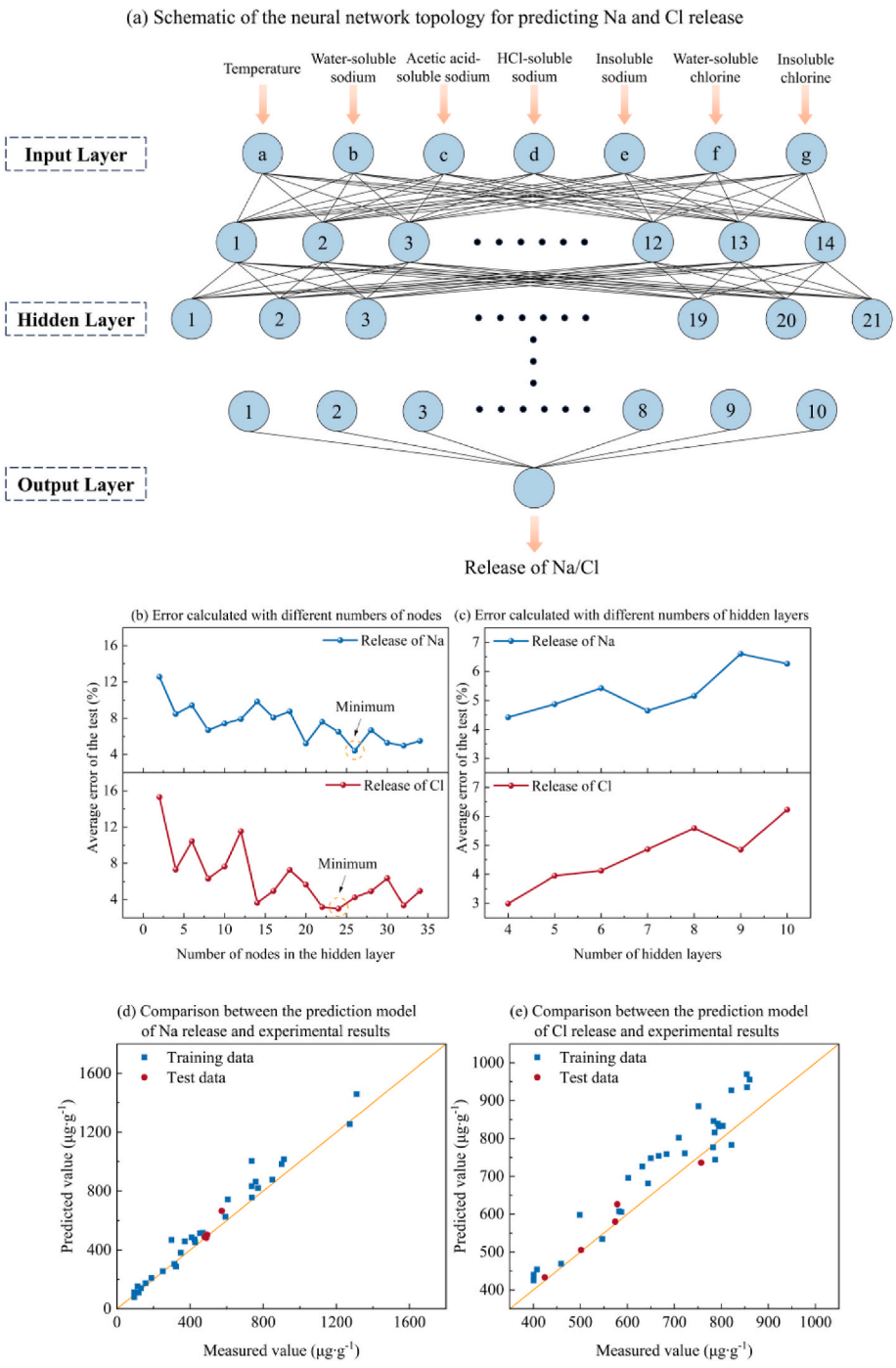

Fig. 9. Neural network model and prediction results.

evaluate the constructed neural network model, K-fold cross-validation was adopted in this study. In the K-fold cross-validation approach, the entire dataset was randomly divided into K equally sized subsets (folds). In each iteration, one fold was used as the validation set to assess the model performance, while the remaining K-1 folds were used for model training. This process was repeated K times, ensuring that each fold was used exactly once as the validation set. By applying K-fold cross-validation during model training and evaluation, the generalization ability and robustness of the neural network model could be effectively ensured. This strategy minimizes the risk of overfitting to a specific subset and provides a more reliable estimate of the predictive capability of the model for unseen data.

The model performance was evaluated based on three statistical metrics: Mean Absolute Error (*MAE*), Root Mean Square Error (*RMSE*), and Mean Absolute Percentage Error (*MAPE*). *MAE* measures the average magnitude of the absolute errors between the predicted and true values, with a smaller *MAE* indicating higher accuracy. *RMSE* evaluates the square root of the average squared differences between the predicted and true values, providing an intuitive assessment of error magnitude, where a lower *RMSE* signifies better precision. *MAPE* reflects the average relative error between the predicted and true values, expressed as a percentage, with smaller *MAPE* values indicating higher model accuracy. The corresponding equations are defined as follows.

$$MAE = \frac{1}{n}\sum_{i=1}^{n}|y_i - \hat{y}_i| \tag{11}$$

$$RMSE = \sqrt{\frac{1}{n}\sum_{i=1}^{n}(y_i - \hat{y}_i)^2} \quad (12)$$

$$MAPE = \frac{1}{n}\sum_{i=1}^{n}\frac{|y_i - \hat{y}_i|}{y_i} \quad (13)$$

In these equations, n represents the number of samples, y_i represents the true value, and $\hat{y}_i$ represents the predicted value. These metrics collectively provide a comprehensive evaluation of the model performance and assist in selecting the optimal number of nodes.

In this study, a 5-fold cross-validation (K = 5) was adopted to balance computational cost and evaluation reliability. Specifically, samples 1–9 were assigned to the first fold, samples 10–18 to the second fold, samples 19–27 to the third fold, samples 28–36 to the fourth fold, and samples 37–45 to the fifth fold. The constructed neural network models were tested with varying numbers of nodes, and the corresponding *MAE*, *RMSE*, and *MAPE* values were calculated. The detailed results are summarized in **Supplementary materials–K-fold Cross-validation**. According to the evaluation results, the models predicting Na and Cl release achieved relatively lower *MAE*, *RMSE*, and *MAPE* values when the number of nodes was set to 26 and 24, respectively. This indicates that the models constructed with these neuron numbers exhibit better prediction performance.

Fig. 9 (d) and (e) show the relationship between the predicted values and measured values of Na and Cl release by the neural network model constructed under the optimal number of nodes. The x-axis represents the measured value obtained by the experiment, and the y-axis represents the predicted value calculated by the model. The closer the predicted value is to the measured value, the better the performance of the constructed model. As can be seen from the figure, the data points are closely distributed near the y = x line, indicating that there is good consistency between the predicted value and the experimental value. The prediction errors of the optimized neural network model for Na and Cl release are 4.63 % and 2.99 %, respectively. These results show that the constructed neural network model has high prediction accuracy and robustness. Future studies could increase the sample size and include data from various coal types to improve prediction accuracy and enhance the robustness of the model for high-sodium coal pyrolysis applications.

In summary, Pearson correlation analysis provides a basis for understanding the individual and combined effects of different Na and Cl forms on their release behavior during pyrolysis. Quantifying the strength and direction of these relationships can help develop targeted pretreatment strategies. This conclusion can effectively control the release of harmful elements during the thermal utilization of high-sodium coal and reduce its industrial production and equipment maintenance costs. The development of a neural network model for predicting Na and Cl release based on coal characteristics and pyrolysis parameters has significant advantages. Compared with traditional empirical models or linear models, neural network models can capture the complex interactions between multiple factors and have higher prediction accuracy. The application of this method can quickly screen and optimize pretreatment and operating conditions, reducing reliance on a large number of experiments. From an engineering perspective, the predictive framework established in this study can help design high-sodium coal pyrolysis systems, minimize slagging and corrosion risks, and promote the intelligent and low-emission utilization of complex fuel resources.

4. Conclusion

This study utilized a fluidized bed reactor to investigate the pyrolysis behavior of low-rank high-sodium coal, focusing on the effects of sodium content and water washing on pyrolysis products. Meanwhile, A neural network model was developed to predict Na and Cl release. This research provides valuable insights into optimizing the pyrolysis process and offers accurate predictions of Na and Cl release. These findings establish a foundation for developing intelligent control systems tailored to the industrial application of high-sodium coal, ultimately promoting cleaner and more sustainable energy production.

(1) **Impact of high-sodium factors on the pyrolysis process.** Non-isothermal thermogravimetric analysis (TGA) of SEH and WS washed for 120 min revealed that the activation energy decreased with increasing conversion ratio. The activation energy of WS pyrolysis (569.10–721.35 kJ mol^{-1}) exceeded that of SEH pyrolysis (524.90–621.10 kJ mol^{-1}), accompanied by higher pre-exponential factors. This increase is attributed to the removal of catalytic components containing alkali metals and minerals during water washing, which modified the reaction pathways.

(2) **Influence on pyrolysis products.** SEH was found to contain substantial amounts of W-Na (5614 μg g^{-1}), insoluble sodium (1825 μg g^{-1}), and W-Cl (6280 μg g^{-1}). Prolonged washing effectively removed a significant portion of water-soluble Na and Cl, with minimal effects on their insoluble counterparts. Post-pyrolysis, extended washing increased char yield and ash fusion temperature while slightly reducing char reactivity and significantly reducing the release of Na and Cl. These effects were more pronounced at elevated pyrolysis temperatures.

(3) **Effect on char properties.** The characteristics of char produced by WS washed for varying times differed markedly. Raman and XRD analyses demonstrated enhanced graphitization, reduced aliphatic content, and improved structural orderliness in chars from extensively washed samples. FTIR results indicated fewer active functional groups in the char from WS pyrolysis, while BET analysis revealed increased adsorption capacity for both SEH and WS with rising pyrolysis temperature. Chars from WS exhibited narrower pore size distributions, lower adsorption capacity, and smaller specific surface areas compared to those from SEH.

(4) **Prediction of Na and Cl release.** Multiple linear regression analysis confirmed that W-Na, hydrochloric acid-soluble sodium, acetic acid-soluble sodium, insoluble sodium, W-Cl, and insoluble chlorine significantly influenced Na and Cl release during pyrolysis. A neural network model was constructed to predict these releases, with optimal hidden layers and node configurations determined through the trial-and-error method. The model achieved strong predictive performance, with errors of 4.63 % for Na and 2.99 % for Cl.

CRediT authorship contribution statement

Zhihua Tian: Writing – original draft, Formal analysis, Data curation. **Ruiqing Jia:** Writing – review & editing, Software, Methodology. **Bin Zhang:** Writing – review & editing, Methodology. **Qinhui Wang:** Writing – review & editing, Project administration.

5. Funding

Thanks for the financial support by the Fundamental Research Funds for the Central Universities (2022ZFJH004).

Declaration of competing interest

The authors declare that they have no known competing financial interests or personal relationships that could have appeared to influence the work reported in this paper.

Acknowledgments

Thanks for the technical and financial support of Dongfang Electric Corporation-Zhejiang University Joint Innovation Research Institute.

Thanks for the financial support by the Fundamental Research Funds for the Central Universities (2022ZFJH004).

Appendix A. Supplementary data

Supplementary data to this article can be found online at https://doi.org/10.1016/j.jclepro.2025.145908.

Data availability

Data will be made available on request.

References

MT/T 1074-2007, Classification for Alkali Metal (Potassium, Sodium) Content in Coal. Beijing: Standards press of China.

Asani, E.O., Gbenga-Degun, M., Ajagbe, S.A., et al., 2023. Triple watermarking scheme for digital images. Journal of Hunan University Natural Sciences 50 (10), 135–144.

GB/T 20475.2-2006, Classification for Content of Harmful Elements in coal-part 2: Chlorine. Beijing: Standards press of China.

Bao, Z., Lu, Z., Chen, J., et al., 2023. Relationships between char reactivity and char structure from a suite of organic model compounds. Fuel Process. Technol. 249, 107852.

Barszcz, W., Łożyńska, M., Molenda, J., 2024. Impact of pyrolysis process conditions on the structure of biochar obtained from apple waste. Sci. Rep. 14, 10501.

Butuzova, L., Razvigorova, M., Krzton, A., 1998. The effect of water on the yield and structure of the products of brown coal pyrolysis and hydrogenation. Fuel (Guildf.) 77 (6), 639–643.

Cao, Z., Zhang, J., Pan, W., 2024. A review on release and transformation behavior of alkali metals during high-alkali coal combustion. Sustain. Energy Technol. Assessments 70, 103966.

Chen, Y., Luo, Z., Fang, M., et al., 2020. Migration and transformation of sodium during staged coal combustion of zhundong coal and influence of carbon coating. Fuel Process. Technol. 203, 106382.

Chen, Y., Wang, C., Li, Y., et al., 2024. Experimental study on metal removal characteristics of Zhundong coal to produce ultra-clean coal using acid-alkali method. Fuel (Guildf.) 364, 131071.

Chen, Z., Liu, J., Jia, D., et al., 2025. Migration and transformation pathways of chlorine and sulfur in producing pyrolytic biochar of a Zn/Cd-remediating plant amended with modified kaolin. Fuel (Guildf.) 383, 133856.

Ding, K., Zhang, C., 2017. Interactions between organic nitrogen and inorganic matter in the pyrolysis zone of underground coal gasification: insights from controlled pyrolysis experiments. Energy (Calg.) 135, 279–293.

Ding, L., Gao, Y., Li, X., et al., 2019. A novel CO_2-water leaching method for AAEM removal from Zhundong coal. Fuel (Guildf.) 237, 786–792.

Draper, N.R., Smith, H., 1998. Applied Regression Analysis[M]. Wiley.

Durbin, J., Watson, G.S., 1992. Testing for serial correlation in least squares regression. I. Breakthroughs in Statistics 237–259.

Gao, Y., Sun, L., Tian, Y., 2024. Pyrolysis characteristics and product distribution of low-rank coal with heat-carrying particles adopting TG-FTIR and a novel self-mixing down tube reactor. Case Stud. Therm. Eng. 54, 104041.

Ge, H., Shen, L., Song, T., et al., 2019. Study on the migration characteristics of sodium and chlorine in chemical looping process of ZhunDong coal with hematite oxygen carrier. Energy Fuels 33 (2), 1489–1500.

Gregg, S.J., Sing, K.S.W., 1982. Adsorption, Surface Area and Porosity[M]. Academic Press, London.

Gritti, F., Guiochon, G., 2007. Comparison between the loading capacities of columns packed with partially and totally porous fine particles: what is the effective surface area available for adsorption? J. Chromatogr. A 1176 (1–2), 107–122.

Guo, Z., Zhang, L., Wang, P., et al., 2013. Study on kinetics of coal pyrolysis at different heating rates to produce hydrogen. Fuel Process. Technol. 107, 23–26.

Guo, S., Zhou, X., Song, S., et al., 2017a. Optimization of leaching conditions for removing sodium from sodium-rich coals by orthogonal experiments. Fuel (Guildf.) 208, 499–507.

Guo, S., Jiang, Y., Yu, Z., et al., 2017b. Correlating the sodium release with coal compositions during combustion of sodium-rich coals. Fuel (Guildf.) 196, 252–260.

Guo, J., Zhang, M., Yan, G., et al., 2023. Removal of AAEMs from high alkali coal under supercritical CO_2 fluid-citric acid extraction system. Energy Sources, Part A Recovery, Util. Environ. Eff. 45 (2), 5836–5847.

Han, L., Zhu, C., Yao, Q., et al., 2022. In-situ catalytic gasification of sodium-rich direct coal liquefaction residue under CO_2 atmosphere and kinetic analysis of gasification reaction process. J. Energy Inst. 101, 233–242.

Hao, J., Xu, F., Yang, D., et al., 2025. Analytical pyrolysis of biomass using pyrolysis-gas chromatography/mass spectrometry. Renew. Sustain. Energy Rev. 208, 115090.

He, X., Wang, W., Yang, Y., et al., 2023a. Occurrence relationship between sodium and maceral groups in subbituminous coal: a case Study on Zhundong coal and Shenfu coal. Minerals (Basel) 13 (1), 122.

He, X., Che, K., Pan, J., et al., 2023b. Occurrence mode of sodium in Zhundong coal, China: relationship to maceral groups. Minerals (Basel) 13 (9), 1155.

Hosokai, S., Matsuoka, K., Kuramoto, K., et al., 2016. Practical estimation of reaction heat during the pyrolysis of cedar wood. Fuel Process. Technol. 154, 156–162.

Hui, S., Lv, Y., Niu, Y., et al., 2021. Effects of leaching and additives on the formation of deposits on the heating surface during high-Na/Ca Zhundong coal combustion. J. Energy Inst. 94, 319–328.

Jiang, F., Zhang, S., Huang, X., et al., 2019. Effect of particle size on sodium distribution and sodium removal by water washing of Zhundong coal. Energy Sources, Part A Recovery, Util. Environ. Eff. 41 (2), 129–136.

Johnson, C.A., Patrick, J.W., Thomas, K.M., 1986. Characterization of coal chars by Raman spectroscopy, X-ray diffraction and reflectance measurements. Fuel (Guildf.) 65 (9), 1284–1290.

Ju, J., You, K., Liu, S., et al., 2022. Effect of water vapor on pore structure, surface functional groups, and combustion performance of pyrolytic semicoke. ACS Omega 7 (28), 24587–24595.

Jüntgen, H., 1984. Review of the kinetics of pyrolysis and hydropyrolysis in relation to the chemical constitution of coal. Fuel (Guildf.) 63 (6), 731–737.

Khatami, R., Levendis, Y.A., 2016. An overview of coal rank influence on ignition and combustion phenomena at the particle level. Combust. Flame 164, 22–34.

Khayet, M., Velázquez, A., Mengual, J.I., 2004. Modelling mass transport through a porous partition: effect of pore size distribution. J. Non-Equilibrium Thermodyn. 29 (3), 279–299.

Li, X., Hayashi, J., Li, C., 2006. FT-Raman spectroscopic study of the evolution of char structure during the pyrolysis of a Victorian brown coal. Fuel (Guildf.) 85 (12–13), 1700–1707.

Li, Q., Wang, Z., He, Y., et al., 2017a. Pyrolysis characteristics and evolution of char structure during pulverized coal pyrolysis in drop tube furnace: influence of temperature. Energy Fuels 31 (5), 4799–4807.

Li, R., Chen, Q., Zhang, H., 2017b. Detailed investigation on sodium (Na) species release and transformation mechanism during pyrolysis and char gasification of High-Na zhundong coal. Energy Fuels 31 (6), 5902–5912.

Li, X., Li, J., Wu, G., et al., 2018. Clean and efficient utilization of sodium-rich Zhundong coals in China: behaviors of sodium species during thermal conversion processes. Fuel (Guildf.) 218, 162–173.

Li, H., Shi, S., Lin, B., 2019. Effects of microwave-assisted pyrolysis on the microstructure of bituminous coals. Energy (Calg.) 187 (15), 115986.

Lin, R., Ritz, G.P., 1993. Studying individual macerals using i.r. micro-spectrometry and implications on oil versus gas/condensate proneness and "low-rank" generation. Org. Geochem. 20 (6), 695–706.

Lin, Y., Li, Q., Ji, K., et al., 2014. Thermogravimetric analysis of pyrolysis kinetics of Shenmu bituminous coal. React. Kinet. Mech. Catal. 113, 269–279.

Lin, D., Qiu, P.H., Xie, X., et al., 2018. Chemical structure and pyrolysis characteristics of demineralized Zhundong coal. Energy Sources, Part A Recovery, Util. Environ. Eff. 40 (3), 282–287.

Liu, Y., Wang, Z., Lv, Y., et al., 2018a. Inhibition of sodium release from Zhundong coal via the addition of mineral additives: a combination of online multi-point LIBS and offline experimental measurements. Fuel (Guildf.) 212, 498–505.

Liu, Y., Wang, Z., Wan, K., et al., 2018b. In situ measurements of the release characteristics and catalytic effects of different chemical forms of sodium during combustion of Zhundong coal. Energy Fuels 32 (6), 6595–6602.

Liu, Y., Wang, Z., Wan, K., et al., 2018c. In situ measurements of the release characteristics and catalytic effects of different chemical forms of sodium during combustion of Zhundong coal. Energy Fuels 32, 6595–6602.

Liu, N., Huang, H., Feng, J., et al., 2025. Effects of alkali and alkaline earth metals in biomass on co-pyrolysis characteristics and product distribution of coal and biomass. Fuel (Guildf.) 389, 134551.

Lou, C., Pu, Y., Zhao, Y., et al., 2021. An in-situ method for time-resolved sodium release behaviour during coal combustion and its application in industrial coal-fired boilers. Proc. Combust. Inst. 38 (3), 4199–4206.

Ma, D., Jia, S., Hu, Z., et al., 2022. Experimental investigation of water washing effect on high-chlorine coal properties. Fuel (Guildf.) 319, 123838.

Ma, D., Li, R., Wang, X., et al., 2025. Chlorine evolution and char characteristics during pyrolysis upgrading of Xinjiang high chlorine coal. Fuel (Guildf.) 379, 133120.

Mazurek, I., Skawińska, A., Sajdak, M., 2021. Analysis of chlorine forms in hard coal and the impact of leaching conditions on chlorine removal. J. Energy Inst. 94, 337–351.

Meng, J., Wang, L., Wang, J., et al., 2023. Characterization and analysis of molecular-scale pore structure of coal with different metamorphic degrees. Energy Fuels 37 (5), 3634–3653.

Muravyev, N.V., Luciano, G., Ornaghi, H.L., et al., 2021. Artificial neural networks for pyrolysis, thermal analysis, and thermokinetic studies: the status quo. Molecules (Basel) 26 (12), 3727.

Nagaraja, S.S., Sahu, A.B., Panigrahy, S., et al., 2021. A fundamental study on the pyrolysis of hydrocarbons. Combust. Flame 233, 111579.

Nagelkerkea, N.J.D., 1991. Note on a general definition of the coefficient of determination. Biometrika 78 (3), 691–692.

Niu, Y., Gong, Y., Zhang, X., et al., 2019. Effects of leaching and additives on the ash fusion characteristics of high-Na/Ca Zhundong coal. J. Energy Inst. 92 (4), 1115–1122.

Obafemi, O., Stephen, A., Ajayi, O., et al., 2019. A survey of artificial neural network-based prediction models for thermal properties of biomass. Procedia Manuf. 33, 184–191.

Occelli, M.L., Olivier, J.P., Perdigon-Melon, J.A., 2002. Surface area, pore volume distribution, and acidity in mesoporous expanded clay catalysts from hybrid density functional theory (DFT) and adsorption microcalorimetry methods. Langmuir 18 (25), 9816–9823.

Oyekunle, D.O., Esseme, A.C.B., Oladipupo, M.A., et al., 2025. Artificial neural network algorithm in nutritional assessment: implication for machine learning prediction in nutritional assessments. Precision Health in the Digital Age: Harnessing AI for Personalized Care, p. 24.

Pal, N., Lim, W.K., 1998. On the coefficient of multiple determination in a linear regression model. Journal of the Italian Statistical Society 7, 129–157.
Patidar, K., Singathia, A., Vashishtha, M., et al., 2022. Investigation of kinetic and thermodynamic parameters approaches to non-isothermal pyrolysis of mustard stalk using model-free and master plots methods. Mater. Sci. Energy Technol. 5, 6–14.
Peng, B., Li, X., Zhao, W., et al., 2018. Study on the release characteristics of chlorine in coal gangue under leaching conditions of different pH values. Fuel (Guildf.) 217, 427–433.
Peng, F., Lu, Y., Wang, Y., et al., 2023. Predicting the formation of disinfection by-products using multiple linear and machine learning regression. J. Environ. Chem. Eng. 11 (5), 110612.
Quast, K.B., 2000. Counter-current ion exchange for the removal of organically bound sodium from low-rank coals. Miner. Eng. 13 (13), 1423–1428.
Quirico, E., Rouzaud, N., Bonal, L., et al., 2005. Maturation grade of coals as revealed by Raman spectroscopy: progress and problems. Spectrochim. Acta Mol. Biomol. Spectrosc. 61 (10), 2368–2377.
Quyn, D.M., Wu, Ho, Li, C., 2002. Volatilisation and catalytic effects of alkali and alkaline earth metallic species during the pyrolysis and gasification of Victorian brown coal. Part I. Volatilisation of Na and Cl from a set of NaCl-loaded samples. Fuel (Guildf.) 81 (2), 143–149.
Shuang, Y., Wu, C., Yan, B., et al., 2010. Heat transfer inside particles and devolatilization for coal pyrolysis to acetylene at ultrahigh temperatures. Energy Fuels 24 (5), 2991–2998.
Sing, K.S.W., Everett, D.H., Haul, R.A.W., et al., 1985. Reporting physisorption data for gas/solid systems with special reference to the determination of surface area and porosity. Pure Appl. Chem. 57 (4), 603–619.
Song, G., Qi, X., Song, W., et al., 2016a. Slagging characteristics of zhundong coal during circulating fluidized bed gasification. Energy Fuels 30 (5), 3967–3974.
Song, G., Qi, X., Song, W., et al., 2016b. Slagging characteristics of Zhundong coal during circulating fluidized bed gasification. Energy Fuels 30 (5), 3967–3974.
Song, W., Song, G., Qi, X., et al., 2017. Speciation and distribution of sodium during Zhundong coal gasification in a circulating fluidized bed. Energy Fuels 31 (2), 1889–1895.
Sun, S., Li, H., Xing, Y., et al., 2023. Impact of atmosphere of dry distillation zone on structure of semi-coke and its CO_2 gasification activity. Coal Chemical Industry 51 (2), 29–32.
Sunphorka, S., Chalermsinsuwan, B., Piumsomboon, P., 2017. Application of artificial neural network for kinetic parameters prediction of biomass oxidation from biomass properties. J. Energy Inst. 90 (1), 51–61.
Swaine, D.J., 1992. The organic association of elements in coals. Org. Geochem. 18 (3), 259–261.
Tang, H., Xu, J., Dai, Z., et al., 2017. Functional mechanism of inorganic sodium on the structure and reactivity of Zhundong chars during pyrolysis. Energy Fuels 31 (10), 10812–10821.
Tay, H., Kajitani, S., Zhang, S., 2013. Effects of gasifying agent on the evolution of char structure during the gasification of Victorian brown coal. Fuel (Guildf.) 103, 22–28.
Tian, Z., Zhang, B., Wang, Q., et al., 2025. Investigation on release and migration characteristics of sodium during the combustion of high-sodium coal with phosphorite. J. Ind. Eng. Chem. 144, 541–551.
Wan, K.D., Xia, J., Wang, Z.H., et al., 2017. Large-eddy simulation of pilot-assisted pulverized-coal combustion in a weakly turbulent jet. Flow Turbul. Combust. 99 (2), 531–550.
Wang, X., Xu, Z., Wei, B., et al., 2015a. The ash deposition mechanism in boilers burning Zhundong coal with high contents of sodium and calcium: a study from ash evaporating to condensing. Appl. Therm. Eng. 80, 150–159.
Wang, C., Jin, X., Wang, Y., et al., 2015b. Release and transformation of sodium during pyrolysis of zhundong coals. Energy Fuels 29 (1), 78–85.
Wang, C., Liu, Y., Jin, X., et al., 2016. Effect of water washing on reactivities and NOx emission of Zhundong coals. J. Energy Inst. 89 (4), 636–647.
Wang, Z.H., Liu, Y.Z., Whiddon, R., et al., 2017. Measurement of atomic sodium release during pyrolysis and combustion of sodium-enriched Zhundong coal pellet. Combust. Flame 176, 429–438.
Wang, Y., Jin, J., Liu, D., et al., 2018. Understanding ash deposition for Zhundong coal combustion in 330 MW utility boiler: focusing on surface temperature effects. Fuel (Guildf.) 216, 697–706.
Wang, T., Li, C., Zhou, B., et al., 2020. Experimental investigation of thermal effect in coal pyrolysis process. Fuel Process. Technol. 200, 106269.
Wang, Z., Wang, Z., Wang, T., 2024a. Research progress on heat effects of coal pyrolysis process. J. Anal. Appl. Pyrolysis 183, 106827.
Wang, K., Ding, J., Deng, J., et al., 2024b. Hydrogen generation mechanism of oil-rich coal oxidation in low temperature. Energy (Calg.) 293 (15), 130739.
Wei, L., Cui, B., Chen, Y., et al., 2019. Occurrence of sodium in high alkali coal and its transformation during combustion. J. Fuel Chem. Technol. 47 (8), 897–906.
Wei, X., Huang, S., Wu, Y., et al., 2022. Effects of demineralization and devolatilization on fast pyrolysis behaviors and product characteristics of penicillin mycelial residues. J. Hazard Mater. 430, 128359.
Wen, C., Zhang, P., Yu, D., et al., 2017. Loading identical contents of sodium and quartz into different ash-removed coals to elaborately investigate the real effects of coal particle combustion on the emission behavior of PM_{10}. Proc. Combust. Inst. 36 (2), 2191–2198.
Wijaya, N., Choo, T.K., Zhang, L., 2011. Generation of ultra-clean coal from Victorian brown coal — sequential and single leaching at room temperature to elucidate the elution of individual inorganic elements. Fuel Process. Technol. 92 (11), 2127–2137.
Wu, X., Zhang, X., Yan, K., et al., 2016. Ash deposition and slagging behavior of Chinese Xinjiang high-alkali coal in 3 MWth pilot-scale combustion test. Fuel (Guildf.) 181, 1191–1202.
Wu, L., Guan, Y., Li, C., et al., 2023. Free-radical behaviors of co-pyrolysis of low-rank coal and different solid hydrogen-rich donors: a critical review. Chemical Engineering Journal 474, 145900.
Xie, Y., You, J., Lu, M., et al., 2019. Raman spectroscopic study of coal samples during heating. Appl. Sci. 9 (21), 4699.
Xu, J., Su, S., Sun, Z., et al., 2016. Effects of steam and CO_2 on the characteristics of chars during devolatilization in oxy-steam combustion process. Appl. Energy 182, 20–28.
Xu, L., Liu, H., Zhao, D., et al., 2018a. Transformation mechanism of sodium during pyrolysis of zhundong coal. Fuel (Guildf.) 233, 29–36.
Xu, L., Liu, H., Zhao, D., et al., 2018b. Transformation and catalytic effects of sodium during coal pyrolysis. Int. J. Energy Res. 42, 4131–4141.
Xu, Y., Chen, X., Wang, L., et al., 2020. Progress of Raman spectroscopic investigations on the structure and properties of coal. J. Raman Spectrosc. 51 (9), 1874–1884.
Yang, Y., Lin, X., Chen, X., et al., 2018. Investigation on the effects of different forms of sodium, chlorine and sulphur and various pretreatment methods on the deposition characteristics of Na species during pyrolysis of a Na-rich coal. Fuel (Guildf.) 234, 872–885.
Yao, Q., Wang, L., Ma, M., et al., 2024. A quantitative investigation on pyrolysis behaviors of metal ion-exchanged coal macerals by interpretable machine learning algorithms. Energy (Calg.) 300, 131614.
Zhang, C., Wang, Y., 2023. The phase and microstructure of lignite char at different pyrolysis temperatures. J. Chongqing Univ. 46 (2), 57–66.
Zhang, J., Sun, Z., Guo, Q., et al., 2017a. Structural changes of Shenfu coal in pyrolysis and hydrogasification reactivity of the char. J. Fuel Chem. Technol. 45 (2), 129–137.
Zhang, L., Hu, S., Chen, Q., 2017b. Molecular structure characterization of the tetrahydrofuran-microwave-extracted portions from three Chinese low-rank coals. Fuel (Guildf.) 189 (1), 178–185.
Zhang, X., Zou, C., Zhao, J., et al., 2019. Effect of H_2 and CO as pyrolysis atmosphere on chemical structure of char by XRD and Raman methods. J. Fuel Chem. Technol. 47 (11), 1288–1297.
Zhang, Z., Zhou, H., Zhou, Q., et al., 2020. Catalytic effect of inherently-water-soluble sodium on Zhundong coal gasification. Sci. Adv. Mater. 12 (7), 1019–1026.
Zhang, T., Li, Z., Hu, F., et al., 2021. Correlation of sodium releasing and mineral transformation characteristics with ash composition of typical high-alkali coals. Fuel Process. Technol. 224, 107035.
Zhang, Z., Zhou, H., Wang, X., et al., 2022a. Influence mechanism of water-soluble sodium on Zhundong coal pyrolysis. ACS Omega 7 (14), 11862–11870.
Zhang, X., Wang, W., Guo, R., et al., 2022b. Study on the effect of pyrolysis conditions on the combustion behavior and char structure evolution. ACS Omega 7 (27), 23634–23642.
Zhao, D., Liu, H., Jiang, L., et al., 2017. Investigation into the relationship between oxygen-containing groups and the release of Na and Cl during preoxidation and pyrolysis of Na-Enriched zhundong coal. Energy Fuels 31 (11), 11939–11946.
Zhao, B., Wang, J., Chen, F., et al., 2014. Hydrothermal treatment to remove sodium from high sodium coal and its influence on combustion characteristics. J. Fuel Chem. Technol. 42 (12), 1416–1422.
Zhao, X., Yang, F., Tan, H., et al., 2024. Effect of the water washing pretreatment on biomass pyrolysis in CO_2 atmosphere. J. Energy Inst. 115, 101697.
Zhou, J., Liu, G., Wang, S., et al., 2020. TG-FTIR and Py-GC/MS study of the pyrolysis mechanism and composition of volatiles from flash pyrolysis of PVC. J. Energy Inst. 93 (6), 2362–2370.
Zhou, R., Gao, Q., Wang, Q., et al., 2025. Machine learning optimization of waste salt pyrolysis: predicting organic pollutant removal and mass loss. Sustainability (Basel) 17 (7), 3216.
Zhu, C., Qu, S.J., Zhang, J., et al., 2017. Distribution, occurrence and leaching dynamic behavior of sodium in Zhundong coal. Fuel (Guildf.) 190, 189–197.
Zhu, C., Tu, H., Bai, Y., et al., 2019. Evaluation of slagging and fouling characteristics during Zhundong coal co-firing with a Si/Al dominated low rank coal. Fuel (Guildf.) 254, 115730.
Zhu, W., Li, X., Sun, R., et al., 2022. Dynamic behaviors of the sodium, calcium and iron release during coal combustion using multi-point LIBS. Combust. Flame 244, 112237.